Effects of transient, persistent, and resurgent sodium currents on excitability and spike regularity in vestibular ganglion neurons

Selina Baeza-Loya[1], Ruth Anne Eatock[2*]

[1]Virginia Merrill Bloedel Hearing Research Center, Department of Otolaryngology-HNS, University of Washington, Seattle, WA, United States

[2]Department of Neurobiology, University of Chicago, Chicago, IL, United States

*** Correspondence:**
Ruth Anne Eatock
eatock@uchicago.edu

Keywords: Vestibular ganglion neurons, spiking, regularity, excitability, Na_V currents, persistent current, resurgent current.

Abstract

Vestibular afferent neurons occur as two populations, regular and irregular, that provide distinct information about head motions. Differences in spike timing regularity are correlated with the different sensory responses important for vestibular processing. Relative to irregular afferents, regular afferents have more sustained firing patterns in response to depolarizing current steps, are more excitable, and have different complements of ion channels. Models of vestibular regularity and excitability emphasize the influence of increased expression of low-voltage-activated potassium currents in irregular neurons. We investigated the potential impact of different modes of voltage-gated sodium (Na_V) current (transient, persistent, and resurgent) in cell bodies from vestibular ganglion neurons (VGNs), dissociated and cultured overnight. We hypothesized that regular VGNs would show the greatest impact of persistent (non-inactivating) Na_V currents and of resurgent Na_V currents, which flow when Na_V channels are blocked and then unblocked. Whole-cell patch clamp experiments showed that much of the Na_V current modes is carried by $Na_V1.6$ channels. With simulations, we detected little substantial effect in any model VGN of persistent or resurgent modes on regularity of spike timing driven by postsynaptic current trains. For simulated irregular neurons, we also saw little effect on spike rate or firing pattern. For simulated regular VGNs, adding resurgent current changed the detailed timing of spikes during a current step, while the small persistent conductance (less than10% of transient Na_V conductance density) strongly depolarized resting potential, altered spike waveform, and increased spike rate. These results suggest that persistent and resurgent Na_V current can have a greater effect on the regular VGNs than on irregular VGNs, where low-voltage-activated K conductances dominate.

Introduction

Vestibular hair cells transmit information about head motions and tilt to the peripheral terminals of bipolar vestibular ganglion neurons (VGNs, Fig. 1A), which project centrally to the brain stem and vestibular cerebellum. VGNs in amniotes are well-known for their differences in spike timing, regular and irregular, that synapse on peripheral and central epithelial zones of origin and correlate with tonic and phasic response dynamics (reviewed in Goldberg, 2000; Eatock and Songer, 2011). The difference in regularity represents different encoding strategies, more "temporal" in the central irregular afferents and more "rate-based" in the peripheral regular afferents, which favor different kinds of sensory information (reviewed in Cullen, 2019). The cellular mechanisms that give rise to the difference in regularity are therefore significant for vestibular information processing. Here we examine whether different modes of voltage-gated sodium current (I-Na_V) – transient, persistent, and resurgent – contribute to spiking excitability and regularity.

Depolarizing current steps evoke a spectrum of firing patterns in isolated VGN cell bodies, ranging from sustained (tonic) to transient (phasic) patterns. Several lines of evidence indicate that sustained and transient firing patterns correspond, respectively, to regular and irregular spike timing *in vivo* (Iwasaki et al., 2008; Kalluri et al., 2010). We investigated the Na_V currents that give rise to firing patterns in dissociated VGN cell bodies, which allow for the high-quality voltage clamp necessary for recording very fast Na_V currents. *In vivo*, spikes initiate in the peripheral neurite at the heminode near its hair cell synapse and travel through the cell body into the central neurite (Fig. 1A). All segments except the synapse become myelinated over the first postnatal week, including the cell body. To gain access for the patch electrode to the VGN membrane beyond the first postnatal week, we cultured dissociated cell bodies overnight, which loosens or eliminates the myelin covering.

With this approach, previous work on rat VGNs in the first two postnatal weeks established that, relative to sustained VGNs, transient VGNs are less excitable, with higher current thresholds for spiking reflecting their more negative resting potentials and lower input resistances (Kalluri et al., 2010). A major factor in these differences is the greater expression by transient VGNs of low-voltage-activated potassium (K_{LV}) channels from the K_V1 and K_V7 channel families. By stimulating VGNs with trains of simulated excitatory postsynaptic currents (EPSCs), Kalluri et al. (2010) showed that greater K_{LV} current produced more irregular timing.

Na_V currents drive the rising phase of most neuronal action potentials (reviewed in Bean, 2007). In rat vestibular ganglia (Liu et al. 2016), we showed diverse expression of Na_V channel subunits and characterized multiple transient Na_V currents (I-Na_VT) in immature VGNs. Here we investigated a different aspect of Na_V current expression that becomes a factor as the inner ear matures: the expression of persistent (Na_VP) or resurgent (Na_VR) Na_V modes of current, which flow through the same channel subunits as produce larger Na_VT currents (Brown et al., 1994; Raman and Bean, 1997).

Most Na_V channels strongly inactivate within milliseconds after depolarization, producing I-Na_VT. In some cases, however, a small fraction does not inactivate even in seconds, creating I-Na_VP. I-Na_VP activates more negatively than I-Na_VT and therefore enhances Na_V channel availability near

resting potential, contributing to excitability and repetitive firing (Crill, 1996; Raman & Bean, 1997; Do and Bean, 2003). In some cases, Na_V channels opened by depolarization are blocked by an intracellular molecule before they inactivate; upon repolarization, the channels rapidly unblock and carry I-Na_VR until they deactivate (Raman & Bean, 1997; Lewis & Raman, 2014).

The Na_VP and Na_VR current modes have been recorded from gerbil calyces, the large terminals formed by vestibular afferents on type I hair cells, where they are attributed to tetrodotoxin (TTX)-sensitive Na_V1.6 channels (Meredith and Rennie, 2020). We speculated that variation in Na_V current modes mediates differences in spiking excitability or regularity in VGNs, as suggested for certain brain neurons (Lewis and Raman, 2014). Our results suggest that in sustained VGNs, Na_VP currents substantially affect spike rate, while in transient VGNs, we found no evidence that Na_VP and Na_VR currents affect regularity or rate.

Materials and Methods

Electrophysiology

Animals: For all electrophysiology experiments, wildtype CD1 mice were obtained from Charles River Laboratories (Wilmington, MA). Mice were housed at the University of Chicago and were handled in accordance with the National Research Council Guide for the Care and Use of Laboratory Animals. All procedures were approved by the animal care committee at the University of Chicago.

Preparation: Whole-cell currents and voltages were recorded from VGNs isolated from mice on postnatal day 3 (P3) to P25 (11 ± 0.5 (SEM) days old, median = 8, n = 146). VGNs from mice of both sexes were pooled into cell cultures; in the few cases where cells were from cultures made of a single sex (n = 7 female, 8 male cells), there were no significant differences in Na_V current voltage dependence of activation ($p = 0.99$, power = 0.05) or conductance density ($p = 0.18$, power = 0.27) between sexes. Mice were anesthetized via isoflurane inhalation and decapitated. Temporal bones were dissected in chilled Liebovitz-15 (L-15) medium supplemented with 10 mM HEPES to pH 7.4, ~320 mmol/kg. Chemicals were purchased from ThermoFisher (Waltham, MA) unless otherwise stated.

Each otic capsule was exposed, and the superior compartment of the vestibular ganglion was dissected out. The ganglion houses the cell bodies of VGNs that synapse on hair cells in the utricle, part of the saccule, and the lateral and anterior semicircular canals, and project centrally to the vestibular nuclei in brain stem and cerebellum. The tissue was placed in L-15 supplemented with 0.12% collagenase and 0.12% trypsin for 15-20 minutes at 37°C. The ganglion was then dissociated by gentle trituration into Minimal Essential Medium with Glutamax supplemented with 10 mM HEPES, 5% fetal bovine serum, and 1% penicillin (Sigma-Aldrich, St. Louis, MO). Cells were allowed to settle in glass-bottomed culture dishes (MatTek, Ashland, MA) precoated with poly-D-lysine. In most experiments, recordings were made after cells were incubated 10-20 hours in 5% CO_2 – 95% air at 37°C. Overnight incubation reduced myelin and satellite cell coverage from cell bodies. Age of cells does not include time in culture: e.g., data from a P17 VGN indicates the pup was 17 days old when neurons were harvested, and the cells were P17 + ~1 day *in vitro*. The number of surviving cells decreased with age.

Recording solutions: During experiments, cells were bathed in one of two external solutions, summarized in Table 1. For voltage clamp experiments, we used a "Na^+-reduced" external solution and a "Cs^+" internal solution, designed to minimize K^+ currents, Ca^{2+} currents, and reduce Na^+ currents. K^+ currents were minimized and Na^+ currents reduced by substituting Cs^+ for K^+ (in both external and internal solutions, Table 1) and replacing about half of the external Na+ with equivalent tetraethylammonium chloride (TEACl, a K channel blocker). By halving the Na_V current, the Na^+-reduced external solution improved voltage clamp quality by reducing voltage errors and clamp time constant. To minimize Ca^{2+} current, only trace Ca^{2+} was present and Mg^{2+} was added to block voltage-gated calcium (Ca_V) channels. For current clamp experiments to gather spiking data, we used more physiological external solution and internal solutions ("standard" solutions, Table 1).

Table 1: Whole-cell recording solutions

External												
in mM	**NaCl**	**KCl**	**CsCl**	**$CaCl_2$**	**$MgCl_2$**	**TEACl**	**NaH_2PO_4**	**D-Glucose**		**HEPES**	**pH**	**Osm** (mmol/kg)
Na^+ Reduced	75	0	5.4	0	2.5	75	0	10		5	7.4	310
Standard	144	5.1	0	1.3	0.9	0	0.7	5.6		10	7.4	310
Internal												
in mM	**KCl**	**CsCl**	**$CaCl_2$**	**$MgCl_2$**	**Na_2 creatine phosphate**	**Mg-ATP**	**Li-GTP**	**Na-cAMP**	**EGTA**	**HEPES**	**pH**	**Osm** (mmol/kg)
Cs^+	0	148	0.8	0	3.5	3.5	0.1	0.1	5	5	7.4	300
Standard	135	0	0.1	0.5	5	3	0.1	0.1	5	5	7.25	285

Table 1 *Whole-cell recording solutions.* pH was adjusted with CsOH for Na^+ reduced external and Cs internal solutions, NaOH for standard external solution, and KOH for standard internal solution.

Whole cell recordings: Cells were visualized at 600X on an inverted microscope equipped with Nomarski optics (IMT-2; Olympus, Lake Success, NY). We chose round cells with diameters >5 µm (range 8 – 25µm). Mean membrane capacitance measured by the amplifier was 15 ± 0.5 (median = 16, n = 135), similar to a sample of mouse VGN data we previously reported (Liu et al. 2016). No correlation between age and cell size was observed. Neurons were distinguished from glia by their shape and the presence of Na_V currents and/or spikes.

Signals were delivered, recorded, and amplified with a Multiclamp 700B amplifier, Digidata 1440A digitizer, and pClamp 11 software (n = 146) (Axon Instruments, Molecular Devices, Sunnyvale, CA), with low-pass Bessel filtering set at 10 kHz and sampling interval set at 5 µs. Signals include voltage steps and ramps, current steps, and synthetically generated frozen trains of excitatory postsynaptic currents (EPSCs) based on recordings from vestibular terminals as previously used by our lab (Kalluri et al., 2010). Electrodes were pulled from soda glass (King Precision Glass, Claremont, CA) to resistances of 3 – 4 MΩ in our solutions and wrapped with parafilm to reduce pipette capacitance. All membrane voltages were corrected offline for a liquid junction potential of either 4.7 (standard solution) or 5.2 mV (reduced solution), calculated with JPCalc software (Barry 1994) in pClamp 11.

The series resistance (R_S) ranged between 3 and 10 MΩ and was compensated by 73 ± 0.9% (n = 134). Recordings were analyzed only when the seal exceeded 1 gigaohm (GΩ) and, if standard

solutions were used, the cell maintained stable membrane potential more negative than −64 mV. After compensation for junction potentials, holding potential in voltage-clamp mode was −65 mV (−64.7 mV in standard solutions, −65.2 mV in Na^+ Reduced/Cs^+ solutions). Input resistance was 712 ± 56 MΩ. Fast Na_V currents are difficult to voltage clamp at body temperature, so we recorded at room temperature (23 – 25°C). For our average cell capacitance (15 pF) and after R_S compensation, the voltage clamp time constant ranged from ~15-50 µs, adequate for recording fast Na_V currents at room temperature (room temperature time-to-peak and inactivation time constants ~1 ms, activation and deactivation time constants <1 ms: Patel et al. 2015; Alexander et al., 2021).

Pharmacology: On the day of experiments, we thawed stock solutions of pharmacological agents: Na_V channel blockers tetrodotoxin (TTX; Enzo Life Sciences, Farmingdale, NY; 2 mM in distilled water) and 4,9-anhydro-tetrodotoxin (4,9-ah-TTX; Alomone Labs, Jerusalem, Israel; 500 µM in methanol), or Na_V channel agonist *Anemonia viridis* toxin 2 (ATX-II; Alomone Labs, Jerusalem, Israel; 100 µM in distilled water). Aliquots were added to 5 mL of external solution for final concentrations of 1 µM TTX, 100 nM 4,9-ah-TTX, and 100 nM ATX-II, chosen to maximize blocking or agonizing effects (Oliveira et al., 2004; Rosker et al., 2007). 1 mg/ml of bovine serum albumin was added to the ATX-II solution to reduce adhesion to the plastic delivery tubing. Toxin-containing solutions were applied via local perfusion (Perfusion Fast-Step, Warner Instruments, Holliston, MA) delivered with a Bee Hive Controller (BASI, West Lafayette, IN). Control and drug solutions flowed through adjacent delivery tubes and a stepper mechanism selected the tube directed at the patched cell. This system allows for no dead volume. Perfusion of control solution at the beginning of each drug series provided additional control for flow effects.

Analysis and statistical treatments Analysis was performed in Clampfit (pClamp 10 or 11, Molecular Devices) and MATLAB 2021b (The MathWorks, Natick, MA). Statistical analyses, curve fitting, and figures were done in Origin Pro 2018 (OriginLab, Northampton, MA). Means ± SEM are presented. In box plots, box indicates SEM, middle line indicates median, open squares indicate the mean, and whiskers mark 5-95 confidence intervals. For comparisons between 2 groups, we tested for normal distribution, homogeneity of variance (Levene's test), and estimated statistical significance with Student's t-test or, if variances were unequal, Welch's t-test. We used paired t-tests for drug effects on individual cells and an alpha level of 0.05 for all statistical tests. To evaluate effect size of significant results, i.e., the difference between the means, we calculated bias-corrected Hedges' g (small effect = 0.2, medium = 0.5, large = 0.8; Durlak, 2009). To compare more than 2 groups, we used one-way ANOVA followed by the Bonferroni test for multiple comparisons.

The voltage dependencies of current activation and inactivation were analyzed for currents collected with R_S voltage error <10 mV at peak current. Activation curves of conductance (G) vs voltage (V) were generated by dividing peak current (I) by the driving force ($V - E_{rev}$) to obtain G. E_{rev} was approximated by the equilibrium potential for Na^+ (E_{Na}) for the specified Na^+ concentrations (Table 1). The resulting G-V curves were generally well described by fitting a simple Boltzmann function using the Levenberg-Marquardt fitting algorithm as implemented in OriginPro:

$$G(V) = \frac{G_{max}}{1 + \exp\left(\frac{V_{act} - V}{s}\right)} \quad \text{Eq 1}$$

where G_{max} is the maximum conductance, V_{act} is the voltage of half-maximal activation, and s is the slope factor.

Inactivation G-V curves were generated by measuring how iterated prepulse voltages affect the conductance evoked by a test pulse (step) in the activation range (–35 or –15 mV). Peak current evoked by the test pulse was divided by driving force, plotted against the iterated prepulse voltage, and fit by a Boltzmann function:

$$G(V) = \frac{G_{max}}{1 + \exp\left(\frac{V - V_{inact}}{s}\right)} \quad \text{Eq 2}$$

with V_{inact} equaling the voltage of half-maximal inactivation.

Coefficient of variation (CV) was used to measure regularity of spike trains and was calculated for a given spike train from the mean and standard deviation of interspike interval (ISI):

$$CV = \frac{\sigma(ISI)}{\mu(\mathrm{ISI})} \quad \text{Eq 3}$$

Because CV varies inversely with spike rate, we manipulated the input current amplitude to hold spike rate approximately constant between control and experimental conditions. Events were counted as spikes when they crossed a voltage threshold, between –20 and 0 mV, which was set for each neuron to exclude subthreshold excitatory postsynaptic potentials (EPSPs). We confirmed that APs and not EPSPs were counted by comparing the waveforms: APs had higher peak values, faster rise times and decays, and, often, afterhyperpolarizations (AHPs, measured as the difference between the resting potential, V_{rest}, and the most negative potential following a spike).

Modeling

A Hodgkin-Huxley model of neuronal firing was used to assess the individual impacts of I-Na$_V$T, I-Na$_V$R and I-Na$_V$P on spiking. The single-compartment model was implemented in MATLAB 2018b and 2021b as a differential equation in which the net current across the neuronal membrane was taken as the sum of various individual currents (Hodgkin and Huxley, 1952):

$$I_{inj} = C_m S \frac{dV}{dt} + I_{Na} + I_{KLV} + I_{KH} + I_H + I_{leak} + I_{EPSC} \quad \text{Eq 4}$$

This model is an extension of the single-compartment VGN model developed by Hight and Kalluri (2016) and Ventura and Kalluri (2019) to fit rat VGN data. Membrane voltage $V(t)$ was solved numerically using a backwards difference method. The specific membrane capacitance (C_m) was fixed at 0.9 μF/cm^2 (Gentet et al., 2000). Cell surface area (S) was fixed to yield a net capacitance of 15 pF, the average for our recorded mouse VGNs. The 5 ionic currents represent key current types in vestibular ganglion neurons: voltage-gated sodium (I_{Na}), low-voltage-activated potassium

(I_{KLV}), high-voltage-activated potassium (I_{KH}), hyperpolarization-activated cyclic nucleotide-gated (I_H), and leak (I_{leak}). The model VGN was stimulated either by injected current steps (I_{inj}) with I_{EPSC} set to 0, or with trains of simulated vestibular excitatory postsynaptic currents (pseudo-EPSCs, I_{EPSC}) with I_{inj} set to 0.

To ensure that the combinations of parameters for currents reproduced APs and firing patterns of different VGNs observed *in vitro* (see Fig. 5A and C), we fit the model output using a local search optimization algorithm. This algorithm compared model APs produced by different combinations of Na_V conductance, K_{LV} conductance, and I_{inj} against an averaged AP (Fig. S1, Table 2). Other parameters (K_H, HCN, and leak conductances) were set to values used by Kalluri and colleagues (see Table 2 for citations). For each firing pattern, the combination of parameters yielding a simulated AP with the lowest mean squared error relative to the average recorded AP was accepted; the resulting simulations are shown in Fig. S1D, E (AP waveforms) and 1F (firing patterns). The model parameter combinations for the 4 identified VGN firing patterns (Fig. S1C, F) are summarized in Table 2.

Table 2: Conductance parameters used for spiking

Firing Pattern	$\bar{g}_{NaT}$, (mS/cm^2)	$\bar{g}_{KLV}$ [a,b,d]	$\bar{g}_{KH}$ [a,c,d]	$\bar{g}_{H}$ [d]	$\bar{g}_{leak}$ [a,d]	V_{rest} (mV)
Sustained-A	20	0	2.8	0.13	0.03	-60.1
Sustained-B	16	0.4	2.8	0.13	0.03	-63.5
Sustained-C	13	0.55	2.8	0.13	0.03	-64.1
Transient	13	1.1	2.8	0.13	0.03	-65.7

Table 2 *Conductance parameters used for model VGNs.* Sources: [a]Hight and Kalluri (2016), [b]Kalluri et al. (2010), [c]Iwasaki et al. (2008), [d]Ventura and Kalluri (2019). g_{NaT} and V_{rest} from this study.

In previous versions of the model (Hight and Kalluri, 2016; Ventura and Kalluri, 2019), I_{Na} was entirely transient (I-Na_VT) and based on the formulation in Rothman and Manis (2003). Here, we adapted I_{Na} to include persistent and resurgent Na_V currents. We used I-Na_VT equations from Hight and Kalluri (2016) and I-Na_VR and I-Na_VP equations from Venugopal et al. (2019) and Wu et al. (2005), substituting our mouse VGN values for conductance density and voltage dependence. Figure 1E shows the *I-V* relations of both recorded and modeled Na_V current components.

The equation for the total Na_V current was based on the computational model by Venugopal et al. (2019) and can be written a:

$$I_{Na} = I_{NaVT} + I_{NaVP} + I_{NaVR} \quad \text{Eq 5}$$

where I_{NaT} , I_{NaP}, and I_{NaR} are modeled:

$$I_{NaVT} = \bar{g}_{NaVT}(m_T{}^3 h_T)(V - E_{Na}) \quad \text{Eq 6}$$

$$I_{NaVP} = \bar{g}_{NaVP}(m_{P_\infty} h_P)(V - E_{Na}) \quad \text{Eq 7}$$

$$I_{NaVR} = \bar{g}_{NaVR}((1 - b_R)^3 h_R{}^5)(V - E_{Na}) \quad \text{Eq 8}$$

Model parameters for Na_V current modes are summarized in Table 3. Conductance densities ($\bar{g}$) cover the range of experimentally derived values from this study on VGN cell bodies and also the data of Meredith and Rennie (2020) on Na_V currents in VGN calyx terminals on hair cells: maximal

persistent conductance ($\bar{g}_{NaVP}$) was set to 2% of the transient conductance ($\bar{g}_{NaVT}$) and the maximum resurgent conductance ($\bar{g}_{NaVR}$) was set to 10% of $\bar{g}_{NaVT}$, as recorded from cell bodies in this study ("VGN" conductance levels), or 4% and 20% respectively, representative of maximum currents recorded in VGN afferent terminals (Meredith and Rennie, 2020) ("calyx" conductance levels).

Table 3: Steady-state parameters for Na_V current modes

		Activation		Inactivation	
	$\bar{g}$ (mS/cm^2)	$V_{1/2}$ (mV)	S (mV)	$V_{1/2}$, (mV)	S (mV)
I-Na$_V$T	12 – 22	-36	6	-68	8
I-Na$_V$P	0.24 – 0.44	-27	10	-52	14
I-Na$_V$R	1.2 – 2.2	-40	22	-40	28

Table 3 *Steady-state activation and inactivation parameters used in modeling Na_V current modes.*

Transient sodium current: The steady-state voltage-dependent activation (m_T) and inactivation (h_T) of Na$_V$T currents are modeled as follows, with voltage of half-activation ($V_{1/2}$) and slope factor (s) set equal to the mean values from this study, similar to previously modeled in Rothman and Manis (2003).

$$m'_T = \frac{m_{T\infty} - m_T}{\tau_{m_T}} \quad \text{Eq 9}$$

$$h'_T = \frac{h_{T\infty} - h_T}{\tau_{h_T}} \quad \text{Eq 10}$$

$$m_{T\infty} = \left[1 + exp\left(\frac{-(V - V_{1/2})}{s}\right)\right]^{-1} \quad \text{Eq 11}$$

$$h_{T\infty} = \left[1 + exp\left(\frac{V - V_{1/2}}{s}\right)\right]^{-1} \quad \text{Eq 12}$$

Steady state voltage-dependent time constants of activation and inactivation functions for Na$_V$T currents, originally from Rothman and Manis (2003), remained mostly unchanged:

$$\tau_{m_T} = 10\left\{5\ exp\left[\frac{V + 60}{18}\right] + 36\ exp\left[-\frac{V + 60}{25}\right]\right\}^{-1} + 0.04 \quad \text{Eq 13}$$

$$\tau_{h_T} = 100\left\{7\ exp\left[\frac{V + 60}{11}\right] + 10\ exp\left[-\frac{V + 60}{25}\right]\right\}^{-1} + 0.6 \quad \text{Eq 14}$$

Persistent and resurgent sodium currents: Steady-state activation (h_P), inactivation (m_P), and voltage-dependent time constant of inactivation (τ_{hP}) for Na$_V$P current are based on Venugopal et al. (2019) and Wu et al. (2005) and are modeled as:

$$m_{P_\infty} = \left[1 + exp\left(\frac{-(V - V_{1/2})}{s}\right)\right]^{-10} \quad \text{Eq 15}$$

$$h'_P = \frac{h_{P_\infty} - h_P}{\tau_{h_P}} \quad \text{Eq 16}$$

$$h_{P_\infty} = \left[1 + exp\left(\frac{V - V_{1/2}}{s}\right)\right]^{-1} \quad \text{Eq 17}$$

$$\tau_{h_P} = 100 + \frac{10000}{1 + exp\left(\frac{V + 60}{10}\right)} \quad \text{Eq 18}$$

The formulation for I-Na$_V$R is from Venugopal et al. (2019). It alters the Hodgkin-Huxley conductance-based formulation to incorporate state-dependent Na^+ resurgence due to unblocking of a channel that was blocked upon opening. The equations that govern voltage-dependent blocking/unblocking (b_R) kinetics are as follows:

$$b'_R = \alpha_b(1 - b_R)b_{R_\infty} - k_b\beta_{b_R}b_R \quad \text{Eq 19}$$

$$b_{R_\infty} = \left(1 + exp\left(\frac{V - V_{1/2}}{s}\right)\right)^{-1} \quad \text{Eq 20}$$

$$\beta_{b_R} = \left(1 + exp\left(\frac{-(V - 40)}{8}\right)\right)^{-2} \quad \text{Eq 21}$$

where constants α_b (0.08) and k_b (0.9) control the rate of unblocking. The voltage-dependent inactivation (h_R) functions include:

$$h'_R = \alpha_{h_R}h_{R_\infty} - 0.8\beta_{h_R}h_R \quad \text{Eq 22}$$

$$h_{R_\infty} = \left(1 + exp\left(\frac{V - V_{1/2}}{s}\right)\right)^{-1} \quad \text{Eq 23}$$

$$\alpha_{h_R} = \frac{1}{1 + exp\left(\frac{-(V + 45)}{8}\right)} \quad \text{Eq 24}$$

$$\beta_{h_R} = \frac{0.5}{1 + exp\left(\frac{-(V + 45)}{15}\right)} \quad \text{Eq 25}$$

Synaptic conductance and EPSC shape: Synaptic input was generated and modeled as described in Hight and Kalluri (2016). Briefly, modeled synaptic events were randomly drawn from Gaussian distributions of size and timing based on EPSC amplitudes and rates. For our model simulations, we simulated EPSCs with a shape based on EPSCs of the lateral extrastriola vestibular afferent calyces in the excised P8 CD1 mouse utricular epithelium at room temperature. These have longer onset and decay times than the standard EPSC shape used in Hight and Kalluri (2016) (Fig. S2). An exponential function was fitted to an averaged synaptic event:

$$s(t) = 3.112 * \exp(-0.4545t) - 3.112 * \exp(-1.121t) \quad \text{Eq 26}$$

Results

Whole-cell ruptured-patch recordings were taken from somata of the vestibular ganglion (VGNs; n = 146) dissociated from CD1 mice of both sexes between P3 and P25 (median = 8) and cultured overnight. VGN cell bodies allow better space clamp than afferents recorded *in vivo*. Because Na_VP and Na_VR current modes are known to upregulate with development (Browne et al., 2017; Hong et al., 2018; Meredith and Rennie, 2020), we needed to record beyond the first postnatal week, by which time myelin is extensive. With overnight culture, VGN cell bodies lose their myelin wrapping, allowing access for recording, but have not yet acquired long neurites that occur with long term culture.

First, we describe Na_VT, Na_VP, and Na_VR current modes recorded from VGNs, and their contributions to voltage dependence and time course of I-Na_V. We then describe experiments investigating contributions of a channel subunit, $Na_V1.6$, known to carry all three current modes. Finally, we examine the roles of each current mode in a computational model of VGN spiking.

Properties of Na_V currents in VGNs

To collect and characterize Na_V currents, we used solutions that lowered R_S voltage errors by decreasing Na_V currents: "Cs^+" internal solution and "Na^+ Reduced" external solution (Table 1), which had Cs^+ instead of K^+ and no added Ca^{2+} to minimized contamination with K^+ or Ca^{2+} current. We recorded at room temperature (~24°C) to slow activation speed of fast Na_V currents into the range for which our voltage clamp time constant is adequate (~15-50 µs, see Methods).

All VGNs had I-Na_VT, some had I-Na_VP, and few had I-Na_VR.

Figure 1 shows exemplar Na_V currents recorded from VGNs in response to voltage protocols previously designed to reveal Na_VT, Na_VP, and Na_VR current components (Stafstrom et al., 1982; Raman and Bean, 1997).

Depolarizing steps following a hyperpolarizing prepulse revealed fast-inactivating I-Na_VT in all VGNs (Fig. 1B), as previously reported (Chabbert et al., 1997; Risner and Holt, 2006; Liu et al., 2016). Table 4 summarizes I-Na_VT properties. I-Na_VT was completely blocked by 1 µM TTX (n = 78). In contrast, in "acute" recordings from immature rat VGNs (P < 8) on the day of dissociation, Liu et al. (2016) recorded multiple kinds of I-Na_VT with different TTX sensitivities and kinetics: TTX-insensitive $Na_V1.5$ current (IC_{50} ~300 nM TTX) and TTX-resistant $Na_V1.8$ current (no block at 5 µM TTX), in addition to TTX-sensitive current. As in other studies of overnight-cultured VGNs (Chabbert et al., 1997; Risner and Holt, 2006; Liu et al. 2016), we did not detect TTX-insensitive or -resistant currents, even with 300 nM TTX to block the large TTX-sensitive currents (n = 5, not shown).

To reveal Na_VP current, we eliminated rapidly inactivating I-Na_VT by applying a slow depolarizing ramp (0.1 mV/ms from −80 to +60 mV) and obtained the TTX-sensitive component by subtracting the ramp current remaining in 1 µM TTX (Fig. 1C). This method often revealed Na_VP current as a small TTX-sensitive inward current activating above –70 mV. I-Na_VP was evident in 42 of 78

(54%) VGNs, P3-25, always in combination with I-Na_VT and in 4 cases with Na_VR current (I-Na_VR) as well.

I-Na_VR was revealed by delivering a depolarizing step to open Na_V channels followed by repolarizing steps to iterated voltage levels (Fig. 1D) (Raman and Bean, 1997). It is thought that a blocking particle enters the channel at the activating voltage and prevents inactivation; with repolarization, the channel unblocks, yielding I-Na_VR, which then inactivates (Bant and Raman, 2010; White et al., 2019). Overall, I-Na_VR was much less common than I-Na_VP, occurring in just 6 of 78 VGNs (8%) tested in voltage clamp. All the cells with I-Na_VR were older than P10; for this age group, the incidence was 6/49 or 12%. Two of the 6 VGNs had I-Na_VT and I-Na_VR but no I-Na_VP. Developmental upregulation of I-Na_VR has been previously described in eight-nerve afferents (Browne et al., 2018; Meredith and Rennie, 2020).

Relative to I-Na_VT, which on average peaked at −20 mV, I-Na_VR and I-Na_VP reached maximal amplitude at –45 mV repolarization voltage and −25 mV ramp voltage, respectively (Fig. 1E). Although, on average, peak I-Na_VP and peak I-Na_VR were just 1% and 3% of peak total I-Na_V, the small Na_VP and Na_VR currents can be relatively much more at subthreshold voltages; for example,

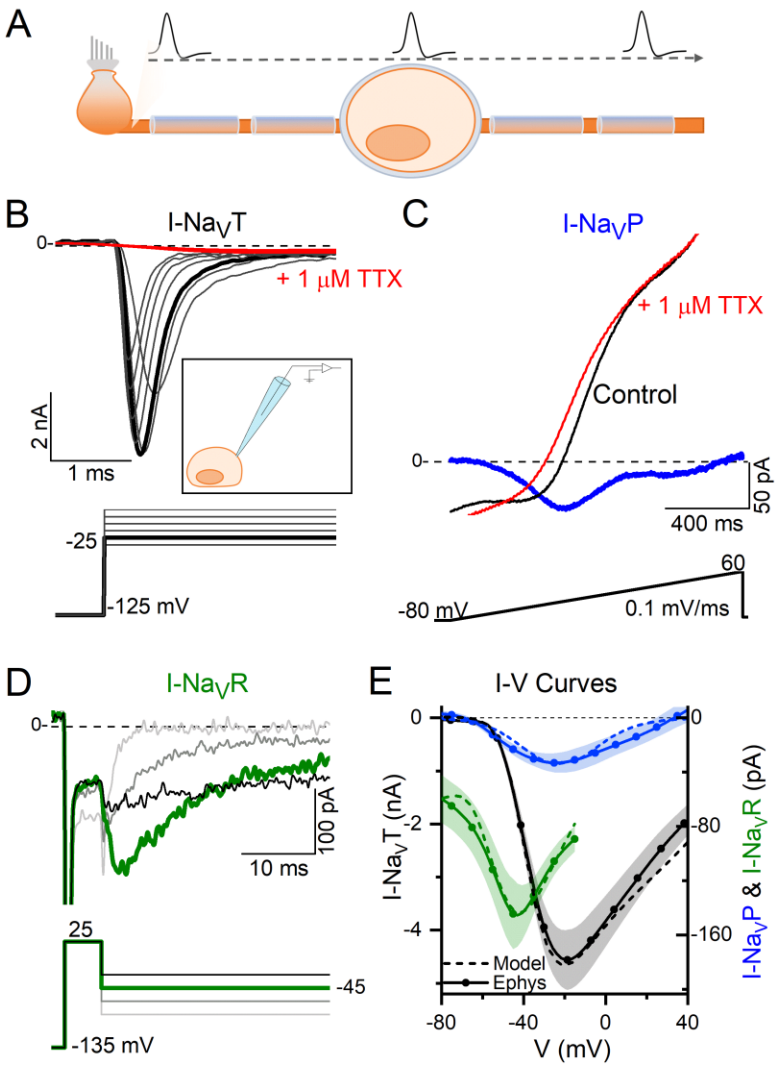

Figure 1 *VGNs expressed Na_VT current, many expressed Na_VP current, and a few expressed Na_VR currents*. **(A)** VGNs are the isolated cell bodies of bipolar vestibular afferents (orange) synapsing on a hair cell (grey). In vivo, APs initiate at a heminode close to the synapse and adjacent to the first myelinated internode and propagate through the myelinated cell body, toward the brain. **(B)** Transient sodium current (I-Na_VT) in a P13 VGN, evoked by stepping up from a prepulse of –125 mV in 5 mV increments. I-Na_VT was always fully blocked by 1 μM TTX. *Inset:* Patching an isolated, demyelinated VGN. **(C)** A small, non-inactivating (persistent) current (I-Na_VP) was isolated from a P3 VGN by applying a 0.1 mV/ms voltage ramp (–80 mV to +60 mV) and subtracting current in 1 μM TTX from control current. **(D)** Resurgent sodium current (I-Na_VR) in a P18 VGN, evoked by applying a +25 mV prepulse followed by repolarizing steps to –25 to –80 mV; and subtracting current in 1 μM TTX from control current. **(E)** I-V curves compared for Na_VT, Na_VP and Na_VR currents. Solid lines (means) plus shading (± SEM) are averaged from recordings; dashed lines show simulated Na_VT, Na_VP and Na_VR currents (see Methods).

from −60 to −50 mV, average I-Na_VP is 13% and I-Na_VR is 124% the peak I-Na_VT over the same voltage range (note that I-Na_VR is present only following a depolarizing pre-pulse).

The addition of I-Na_VP and I-Na_VR affects overall activation voltage.

Cells with I-Na_VR had larger average peak current density (Fig. 2A; collected with the protocol shown in Fig. 1A) relative to VGNs with both Na_VT and Na_VP currents (I-Na_VT + P) or just I-Na_VT. The 2 VGNs with I-Na_VT + R are shown separately in Figure 2A and B and had relatively large current densities and negative midpoints of activation and inactivation.

To measure how the presence of Na_VP and Na_VR currents influenced the voltage dependence of the total I-Na_V, we fit activation (peak G-V) curves with Boltzmann functions (Eqs. 1 and 2; Fig. 2B) and compared fit parameters (Table 4). $V_{1/2,\ Inact}$ did not differ significantly across groups (Table S1). No difference was detected in $V_{1/2,\ Act}$ values between VGNs with I-Na_VT and I-Na_VT + P; although the power is low, the lack of clear difference is not surprising given the small size of I-Na_VP (Table S1). Cells with I-Na_VR (n = 6), however, had $V_{1/2,\ Act}$ values shifted significantly negative to cells with I-Na_VT + P or just I-Na_VT (Fig. 2B, Table S1). The negative shift of activation voltage suggests that I-Na_VR may decrease the current threshold for spiking, possibly by reducing overall rates of inactivation.

In Figure 2C, peak current density values have been converted to maximum Na_V conductance density. Cells with I-Na_VR had greater total Na_V conductance density relative to I-Na_VT and I-Na_VT + P (Table 4). This indicates that VGNs with multiple current modes have a greater I-Na_V conductance. Later (see Fig. 9), we use the computational model to compare the effects of increasing total conductance with just I-Na_VT current vs. I-Na_VT + P and/or R modes.

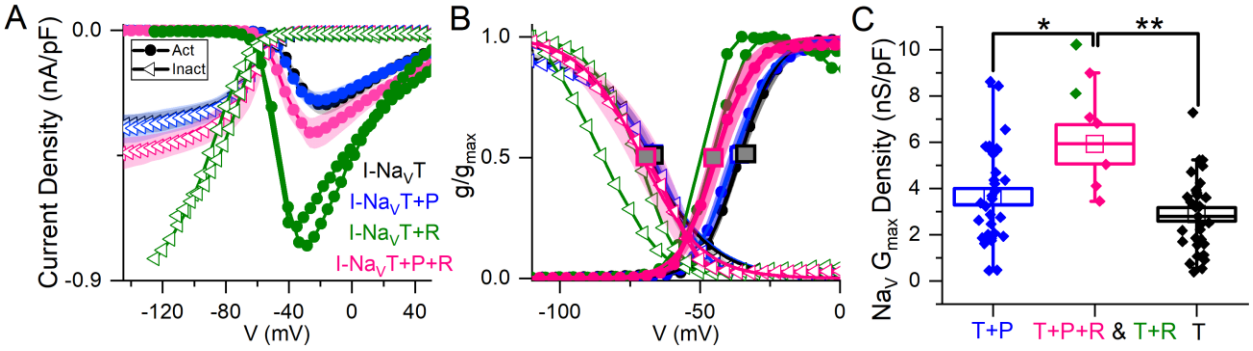

Figure 2 *VGN with different combinations of Na_VT, Na_VP and/or Na_VR current modes differ in their voltage dependence*. **(A)** I-V curves averaged for cells with different current modes. 2 VGNs with I-Na_VT plus I-Na_VR (green) had large current densities and are shown individually. **(B)** G-V (activation) curves show that voltage dependence differed in cells with different combinations of Na_V current modes. $V_{1/2}$ of activation and inactivation is marked with square symbols. Voltage dependence of activation was more negative in VGNs with I-Na_VR (I-Na_VT+R and I-Na_VT+P+R) than I-Na_VT+P ($p = 0.02$) and I-Na_VT ($p = 0.007$). $V_{1/2}$ of inactivation did not differ (one-way 3-factor ANOVA, $p = 0.7$). **(C)** VGNs with I-Na_VR, I-Na_VT+P+R (pink) and I-Na_VT+R (green), had larger (pooled) conductance densities than VGNs without I-Na_VR: I-Na_VT+P (one-way 3-factor ANOVA, $p = 0.02$) and I-Na_VT ($p = 0.002$).

Major fractions of Na_VT, Na_VP, and Na_VR currents flow through Na_V1.6 channels.

In neurons with resurgent currents, such as cerebellar Purkinje cells, $Na_V1.6$ channels can carry all three current components (Raman et al., 1997). Purkinje neurons in $Na_V1.6$ null mice have reduced Na_VT and Na_VP current, and almost no Na_VR current (Raman and Bean, 1997; Raman et al., 1997; Khaliq et al., 2003; Do and Bean, 2004). We tested for $Na_V1.6$ contributions to the Na_VT, Na_VP, and Na_VR current components using the $Na_V1.6$ blocker, 4,9-ah-TTX, at a dose (100 nM) that is ~10-fold higher than the IC50 (IC50 8 nM; Rosker et al., 2007) and still highly selective for $Na_V1.6$ relative to other subunits.

In Na^+ reduced external solution, 100 nM 4,9-ah-TTX blocked approximately 70% of I-Na_VT in VGNs (Fig. 3A, B). Blocked and control currents had similar $V_{1/2}$ values for activation and inactivation (Table 4). This is not surprising, given that the blocked current makes up most of the total current. $V_{1/2,Inact}$ was, however, more negative for the unblocked (residual) current than for control current; $V_{1/2,Act}$ was not significantly different (Table S1). This suggests the possibility of a second TTX-sensitive current that is not carried by $Na_V1.6$ channels and has a more negative inactivation voltage dependence. The voltage dependencies of inactivation and activation of the

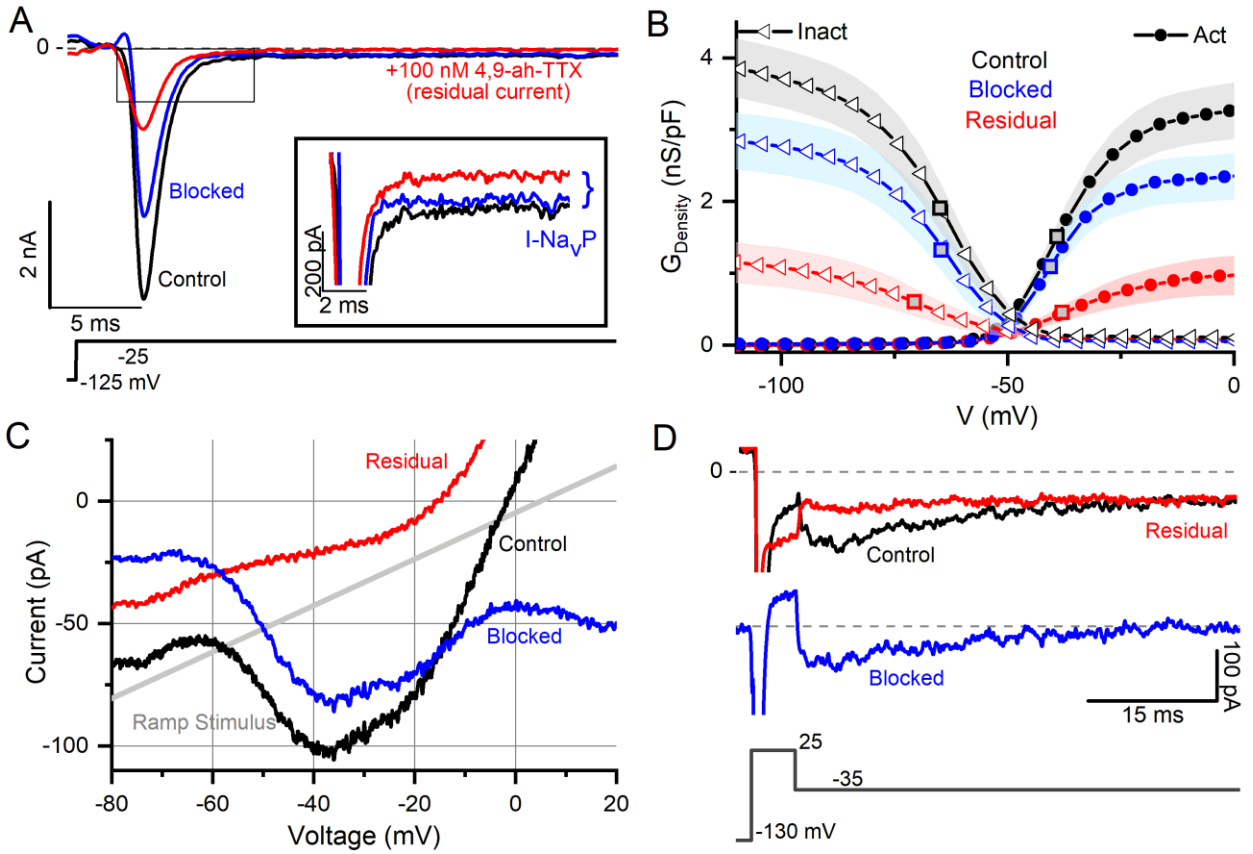

Figure 3 *$Na_V1.6$-selective channel blocker (4,9-ah-TTX) reveals strong $Na_V1.6$ contribution to Na_VT, Na_VP, and Na_VR current modes.* **A)** I-Na_VT (P6 VGN) by 100 nM 4,9-ah-TTX is blocked by ~70% (n = 13). Inset highlights block of Na_VP current during voltage step. **(B)** Boltzmann fits of G-V activation and inactivation curves for data from (A). Square symbols indicate $V_{1/2}$ values. 4,9-ah-TTX-insensitive current (red) had more negative inactivation $V_{1/2}$ (n = 12, p = 0.02, Table 4). **(C & D)** Na_VP (C, P17 VGN) and Na_VR (D, P18 VGN) currents are also blocked (~90%) by 100 nM 4,9-ah-TTX.

two TTX-sensitive, transient conductances (blocked putative $Na_V1.6$ and residual non-$Na_V1.6$) are consistent with observations on isolated rat VGNs (Liu et al., 2016).

Na_VP and Na_VR currents were also blocked by 100 nM 4,9-ah-TTX. Block of I-Na_VP was seen in responses to voltage steps (Fig. 3A inset) or to the slow voltage ramp (Fig. 3C) (n = 13). 4,9-ah-TTX was tested on 1 of the 6 VGNs with Na_VR and produced a strong block of I-Na_VR (Fig. 3D). These results with an $Na_V1.6$-selective blocker suggest that $Na_V1.6$ channels carry the majority of I-Na_V in cultured VGNs, including ~50-70% I-Na_VT and >90% of I-Na_VP and (possibly) most of I-Na_VR, as observed in calyx terminals (Meredith and Rennie, 2020).

I-Na_VT and I-Na_VP were enhanced by Na_V channel agonist ATX-II.

The sea anemone toxin ATX-II interacts with Na_V channel gating, slowing down or preventing inactivation and thereby increasing Na_V current (Oliveira et al., 2004). ATX-II enhances Na_VP current in vestibular afferent calyces (Meredith and Rennie, 2020) and Na_VR and Na_VP currents in spiral ganglion neurons (Browne et al., 2017) and dorsal root ganglion neurons (Klinger et al., 2012). We tested the impact of ATX-II on I-Na_V modes in mouse VGN cell bodies.

100 nM ATX-II increased maximum I-Na_VT in 3 of 7 VGNs tested (Fig. 4A). In all VGNs, inactivation of I-Na_VT was slowed, resulting in increased I-Na_VP at the end of depolarizing steps (Fig. 4A) and during voltage ramps (Fig. 4B). On average, I-Na_VP increased more than 5-fold; the example in Figure 4B was the largest effect seen. We detected no significant difference with ATX-II in activation and inactivation $V_{1/2}$ values for I-Na_VP (Fig 4B) and I-Na_VT (Table 4, Table S1). ATX-II increased the slope factor of inactivation of I-Na_VT ($p = 0.009$, Hedges' $g = 0.85$, large effect) but not activation ($p = 0.85$, power = 0.05) (not shown). We were not able to test ATX-II on resurgent current due to its low incidence.

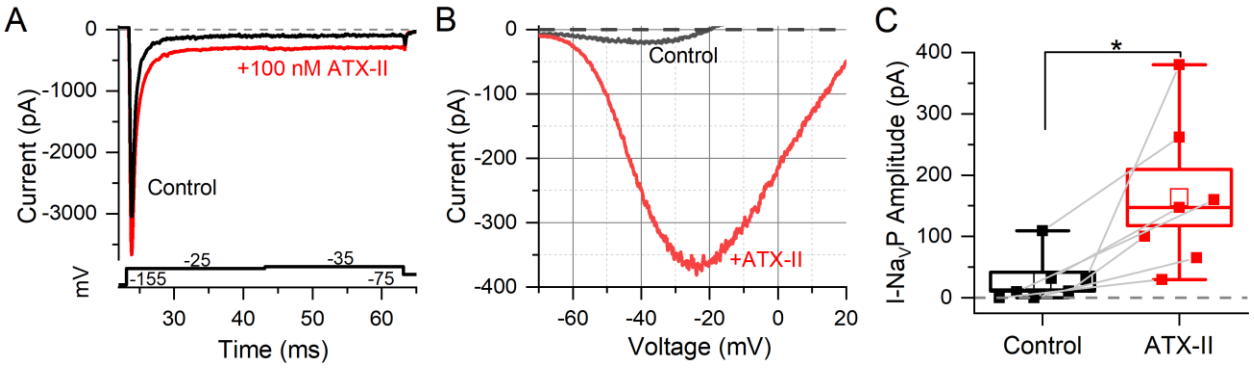

Figure 4 *Na_V channel agonist (ATX-II) strongly enhanced Na_V T and Na_V P currents*. **(A)** An example of enhanced Na_VT and Na_VP current by 100 nM ATX-II (red trace) (top panel) as elicited by depolarizing voltage steps (bottom panel). **(B)** I-V relation of Na_VP current in a P7 VGN, before (grey) and in (red, 100 nM ATX-II); voltage dependence of Na_VP was not significantly altered by ATX-II: $V_{1/2}$ of G-V curves –38.8 ± 4.2 mV (n = 7) vs. –30.6 ± 2.9 mV, p = 0.12, power = 0.33. **(C)** Na_VP currents grew in ATX-II from 27.4 ± 14.4 pA to 163.5 ± 45.9 pA (n = 7, paired t-test; p = 0.01; Hedges' g = 0.93, large effect). Na_VR currents were not tested.

Table 4: Electrophysiological properties of Na_V currents in VGNs						
		Activation		Inactivation		
		$V_{1/2}$ (mV)	S (mV)	$V_{1/2}$ (mV)	S (mV)	G density (nS/pF)
Na_V current	I-Na_V (Na+ Red Ext Sol'n)	-35.8 ± 0.7 (n = 75)	5.7 ± 0.2 (76)	-68.1 ± 1.1 (73)	8.4 ± 0.5 (74)	3.8 ± 0.3 (74)
	I-Na_V (Standard Ext Sol'n)	-38.9 ± 1.2 (29)	3.2 ± 0.3 (29)	-59.1 ± 1.6 (23)	4.4 ± 0.8 (23)	6.8 ± 0.7 (29)
	I-Na_V *(Liu et al., 2016, rat VGN)*	*-36.5 ±1.6 (11)*	*5.7 ±0.4 (11)*	*-76.3 ±0.2 (12)*	*7.6 ±0.1 (12)*	*8.7 ±1.0 (12)*
I-Na_V modes (Figure 2B)	I-Na_V (T)	-35.6 ± 1.0 (10)	6.6 ± 0.3 (10)	-70.1 ± 2.1 (10)	12.3 ± 1.3 (10)	2.9 ± 0.3 (31)
	I-Na_V (T+P)	-37.7 ± 1.6 (12)	7.1 ± 0.4 (12)	-66.4 ± 2.3 (12)	12.8 ± 0.8 (12)	3.6 ± 0.4 (34)
	I-Na_V (T+P+R)	-48.6 ± 5.7* (6)	6.0 ± 0.4 (6)	-67.5 ± 6.3 (6)	11.5 ±1.0 (6)	5.9 ± 0.9* (6)
4,9-ah-TTX (Figure 3B)	Control (I-Na_V)	-38.7 ± 1.3 (12)	5.7 ± 0.5 (12)	-68.3 ± 2.6 (12)	9.1 ± 1.4 (12)	3.1 ± 0.4 (13)
	Subtraction	-39.4 ± 1.6	4.7 ± 0.6	-68.4 ± 2.4	8.8 ± 1.3	2.4 ± 0.3
	Residual	-42.3 ± 2.3	9.2 ± 2.1	-80.6 ± 3.8*	14.5 ± 4.9	0.9 ± 0.3*
ATX-II (Figure 4)	Control (I-Na_V)	-37.7 ± 1.2 (7)	5.7 ± 0.3 (7)	-76.7 ± 3.6 (7)	11.2 ± 0.8 (7)	3.7 ± 1.7 (7)
	ATX-II	-38.7 ± 1.3	5.8 ± 0.1	-80.9 ± 2.9	16.3 ± .3*	1.9 ± 0.4

Table 4 Electrophysiological properties of Na_V currents in VGNs. Asterisks indicate significance in one or two comparisons. See Table S1 for full summary of statistical analyses.

Roles of Na_V currents during action potentials and spike trains

To characterize AP waveforms and firing patterns evoked by current steps and trains of simulated EPSCs, we recorded from 62 VGNs in current clamp mode in our K^+ based standard solutions (Table 1). In these conditions, I-Na_V can escape voltage clamp as it is very large and fast, obscuring the small, non-inactivating Na_VP and Na_VR currents. Although we could not identify I-Na_VP or I-Na_VR in whole-cell recordings in standard solutions, we characterized some features of I-Na_VT and tested for effects of an Na_V channel blocker on spike waveform and firing pattern using.

Na_V conductance correlated with features of action potential waveform.

We classified VGNs into four groups based on firing patterns evoked by depolarizing current steps, following the scheme of Ventura and Kalluri (2019) (Fig. 5A). Transient neurons fired 1 or 2 spikes at step onset independent of step size. Sustained-firing neurons displayed varying degrees of accommodation, ranging from spike trains lasting the duration of the 500-ms depolarizing step (sustained-A type), to shorter trains with faster accommodation (sustained-B), to spiking of 2 or more small spikes that devolve into voltage oscillations (sustained-C).

Transient VGNs had a significantly higher current threshold for spiking relative to sustained-A and sustained-B VGNs but we detected no significant difference in resting potential (V_{rest}), input resistance (R_{in}), or membrane capacitance (C_m) across firing patterns (Table S2). While the incidence of the transient firing pattern was stable with age, at ~50%, the distribution of sustained

firing patterns changed from an approximate balance across sustained-A, -B, and -C subtypes for ages below P10 (n = 21) to mostly sustained-B above P10 (6/7) (Fig. S3A). These changes resemble changes reported in firing pattern with age in rat VGNs (Ventura and Kalluri, 2019).

We assessed the AP waveform associated with each firing pattern (Fig. 5C, summarized in Table 5, and detailed in Table S3). APs from transient VGNs were shorter than APs from sustained-A VGNs (ΔV_{AP}, Fig. 5C) and had slower peak rates of depolarization (peak dV/dt) than APs from sustained-A and sustained-B VGNs (Fig. 5F). Time-to-peak and voltage threshold of APs did not differ significantly across firing patterns (Fig. 5C, D).

For 56 cells, we also collected Na_V currents in voltage clamp and fit activation (peak G-V) curves (Eq. 1) to measure maximum Na_V conductance density (Na_V G_{Max} density) (Fig. 5B). We had hypothesized that Na_V G_{Max} density would be highest for sustained-A VGNs and lowest for

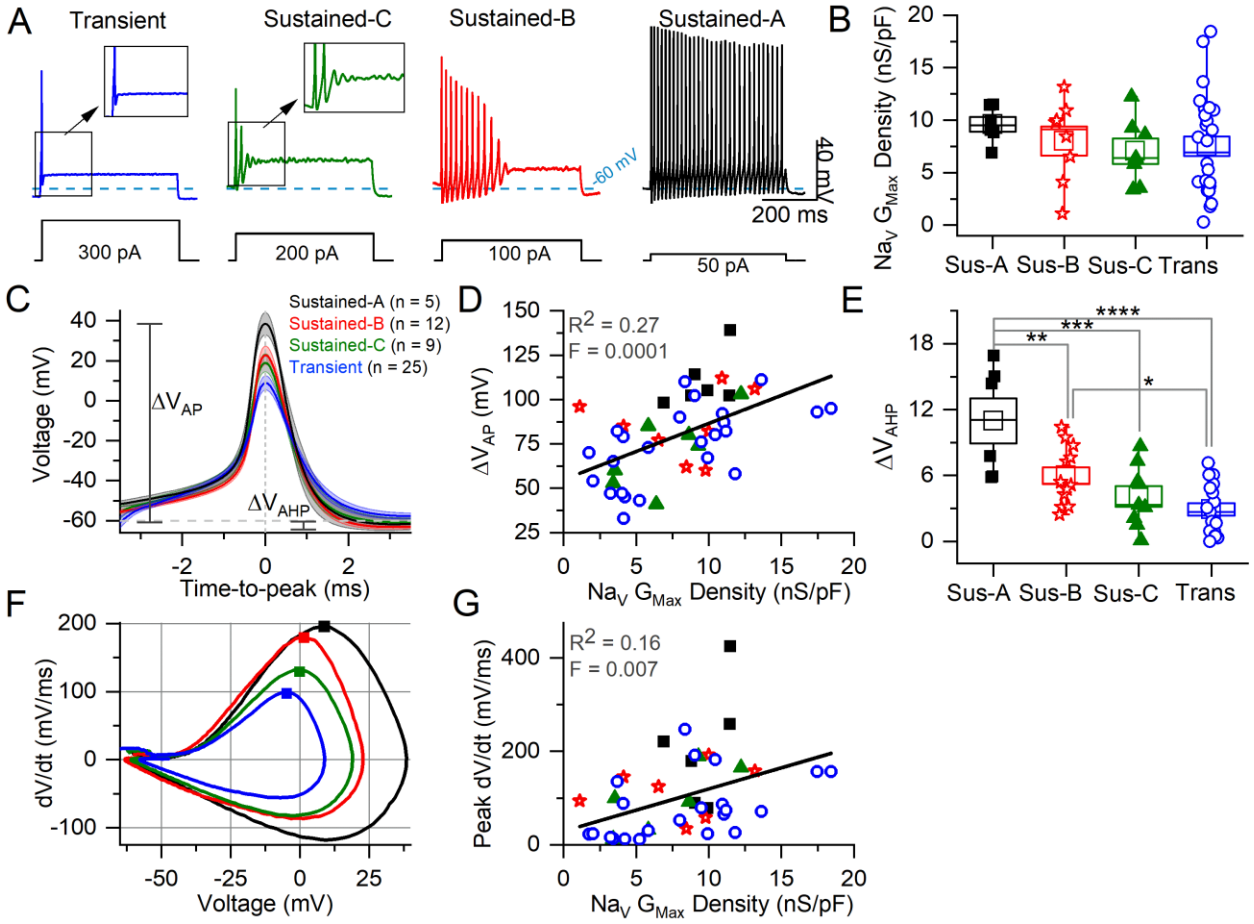

Figure 5 *Correlating VGN firing patterns with spike waveforms and maximum Na_V conductance density.* **(A)** Exemplar firing patterns in VGNs evoked by a 500-ms current steps of different size reflecting different current thresholds. **(B)** Variation in maximum Na_V conductance density with firing pattern is not significant (homogeneous variance, Levene's Test). **C:** Average spikes for each firing pattern, aligned to peak; spike height (ΔV_{AP}) and afterhyperpolarization (V_{AHP}) are measured from V_{rest}. **(D)** AP height correlated weakly with Na_V G_{max} density. **(E)** AHP depth varied with firing pattern (****, p = 0.00007; ***, p = 0.0005; **, p = 0.009; *, p = 0.04). **(F)** Phase plane plots of averaged APs from C. Squares denote peak dV/dt (rate of spike rise) values. **(G)** Peak dV/dt (see squares in F) correlated weakly with Na_V G_{Max} density.

transient VGNs, but did not detect a significant difference in Na_V G_{Max} density across firing pattern populations, although this was a low-powered observation (Fig. 5B, Table 5). Spike height (ΔV_{AP}, Fig. 5C) and peak dV/dt from phase plane plots (Fig. 5F; Bean, 2007) both correlated with Na_V G_{Max} density (Fig. 5D, G), as expected given that Na_V currents drive the rising phase of the AP. We saw no relationship between Na_V G_{Max} density and age (Fig. S3B).

The depth of the spike afterhyperpolarization (AHP) relative to resting potential (ΔV_{AHP}) was significantly greater in sustained-A neurons than any other firing groups (Fig. 5E, Table 5, Table S3). The AHP preserves sodium channel availability by relieving inactivation, shortening the refractory period, and allowing sustained and regular firing at high rates (Gittis et al., 2010). Differences in AHP have previously been attributed to differences in K_{LV} conductance that affect resting potential, current threshold, and membrane recovery time (Hight and Kalluri, 2016; Kalluri et al., 2010; Iwasaki et al., 2008).

In summary, maximum Na_V conductance density did not clearly vary with firing pattern but correlated with features of the spike waveform. We had hypothesized that sustained-A VGNs would have the highest Na_V G_{Max} densities and transient VGNs the lowest densities but did not detect a significant difference in Na_V G_{Max} density across firing pattern populations, although this was a low-powered observation (Fig. 5B, Table 5). Key features of the AP waveform – spike amplitude, AHP, and peak rate of depolarization – did positively correlate with Na_V G_{Max} density (Fig. 5).

Table 5: AP waveform difference between firing patterns (one-way 4-factor ANOVA)

Firing pattern (Figure 5)	Time-to-peak (ms)	AHP (mV)	V_{AP} (mV)	Voltage threshold (mV)	Peak dV/dt (mV/ms)	Na_V G_{max} Den (nS/pF)
Sustained-A	4.5 ± 0.4	11.0 ± 2.0	110.0 ± 6.2	-41.0 ± 3.3	208.3 ± 52.2	9.6 ± 0.7
Sustained-B	4.7 ± 0.3	6.0 ± 0.8	83.5 ± 6.4	-44.3 ± 1.1	166.3 ± 34.2	8.0 ± 1.4
Sustained-C	4.5 ± 0.3	4.1 ± 0.9	80.0 ± 7.7	-44.0 ± 1.3	123.7 ± 28.3	7.0 ± 1.2
Transient	4.2 ± 0.2	2.9 ± 0.6	75.1 ± 4.0	-42.9 ± 1.3	78.6 ± 12.5	7.5 ± 0.9
p	0.45	0.00001	0.009	0.16	0.005	0.68
power	0.23	0.99	0.83	0.16	0.88	0.14

Table 5 *AP waveform differences between firing patterns.*

Blocking $Na_V1.6$ currents reduced excitability and altered AP waveform.

We probed the effects of the $Na_V1.6$ blocker 4,9-ah-TTX on spiking (Figs. 6 and 7), which greatly reduced Na_VT, Na_VP, and Na_VR currents recorded in Na^+ Reduced/Cs^+ solutions (Fig. 3). In standard recording conditions, 100 nM 4,9-ah-TTX showed a similar percent block of I-Na_VT for transient VGNs (50.1 ± 11.3%) and sustained VGNs (52.0 ± 5.2%). Note that this block is close to the % block by the same concentration of 4,9-ah-TTX on I-$Na_V1.6$ expressed in HEK cells (Denomme et al., 2020), and is therefore consistent with $Na_V1.6$ channels carrying most of the Na_V current in our isolated and cultured VGNs.

For step-evoked firing, 100 nM 4,9-ah-TTX affected firing quantitatively, as shown for an exemplar sustained-A neuron (Fig. 6A) and transient neuron (Fig. 6B). For all 13 VGNs tested,

the $Na_V1.6$ blocker increased current threshold for 500-ms steps. In general, for sustained VGNs, 4,9-ah-TTX reduced the number of APs at spiking threshold and throughout the family of current steps. For transient VGNs, 100 nM 4,9-ah-TTX increased current threshold for spiking and decreased spike amplitude (Fig 6B).

To assess changes in the AP waveform, we temporally aligned the peaks of the first APs evoked by long current steps (Fig. 6C, detailed in Table S4). 4,9-ah-TTX reduced spike height by ~20 mV (~25%) on average (Fig. 6D). AHP depth was also reduced, presumably because hyperpolarizing

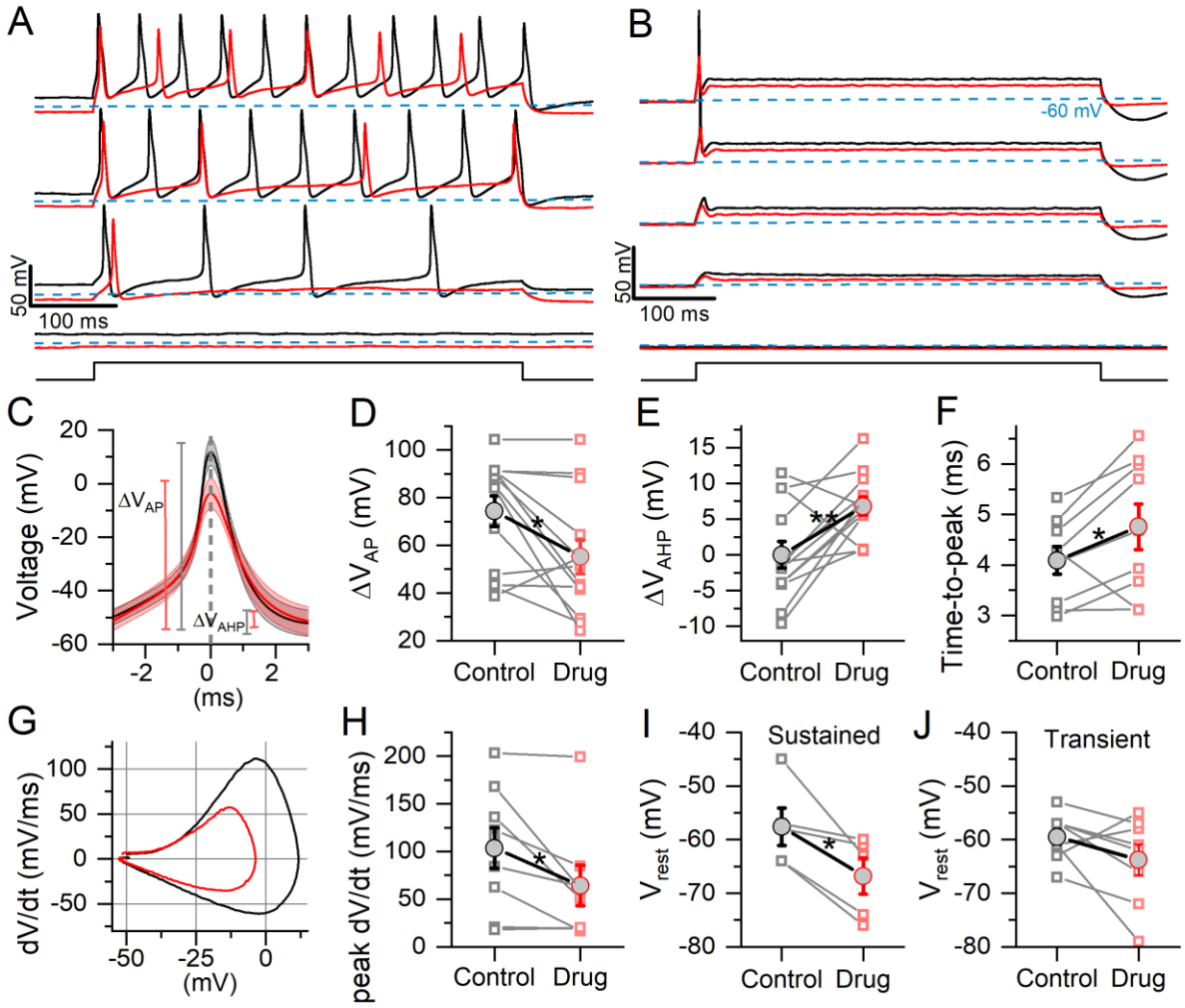

Figure 6 *4,9-ah-TTX reduced step-evoked spiking excitability and altered the AP waveform.* In 100 nM 4,9-ah-TTX, the 50% block of I-Na_VT was similar in transient VGNs (n = 8) and sustained VGNs (n = 5: 1 sustained-A, 1 sustained-B, 3 sustained-C) (Welch's t-test, p = 0.94, power = 0.05). **(A & B)** In 100 nm 4,9-ah-TTX (red), current threshold increased in a sustained-A VGN (A) and a transient VGN (B). In 7 cells, threshold increased from 92.3 ± 14.8 pA to 165.4 ± 23.6 pA (paired t-test, p = 0.002, Hedges' g = 0.63; medium effect). **(C)** First AP from firing patterns such as (A) and (B), averaged (n = 7). **(D)** In 4,9-ah-TTX, spike height decreased (p = 0.01), **(E)** afterhyperpolarization depth increased (p = 0.006), **(F)** and spike latency (i.e., time-to-peak) increased (p = 0.05). In some cases, AHP was depolarized relative to (V_{rest}) by the current step. **(G)** Phase plane plots of mean AP waveforms in (C) highlight the change in peak dV/dt and V_{AP}. **(H)** Peak dV/dt, from (E), was decreased by 4,9-ah-TTX (p = 0.03, Hedges' g = 0.14, small effect). **(I & J)** Sustained VGNs (I) were significantly hyperpolarized (p = 0.03, Hedges' g = 0.67, medium-large effect) but not transient VGNs (J) (p = 0.16).

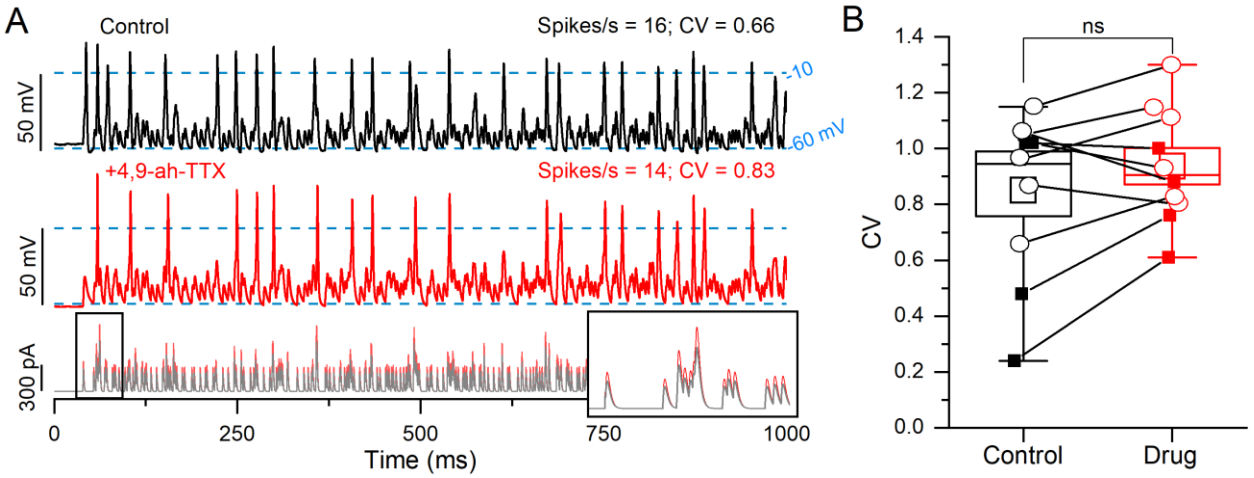

Figure 7 *Reduction in Na_V currents with 4,9-ah-TTX did not significantly affect CV in EPSC-evoked spike trains.* **(A)** 100 nm 4,9-ah-TTX (*red middle panel*) did not significantly reduce CV in spike trains evoked by pseudo-EPSCs (bottom panel) relative to control conditions (*black top panel*) in a P5 transient VGN. Dashed lines at –10 mV indicate event threshold for spike count; dashed lines at –60 mV indicate V_{rest}. *Inset:* first 50 ms of EPSC train. **(B)** CV was not significantly altered in 4,9-ah-TX (paired t-test, 0.85 ± 0.09 vs 0.94 ± 0.07, p = 0.15, power = 0.29). Sustained VGNs (n = 4, *filled squares*); transient VGNs (n = 6, *open circles*).

K^+ currents were less activated during the smaller spike (Fig. 6E) and AP time-to-peak increased (Fig. 6F). No change was detected in spike width at half-height, although control spikes are narrower at their peaks, reflecting their higher rates of depolarization and repolarization (Fig. 6G, H).

4,9-ah-TTX substantially hyperpolarized V_{rest} in sustained VGNs (Fig. 6I) but not transient VGNs (Fig. 6J). These data suggest that in sustained VGNs, 4,9-ah-TTX blocks depolarizing channels that are open at rest, such as I-Na_VT and I-Na_VP. The larger impact of the blocker on sustained VGNs may reflect a different balance of channels open at rest: they have smaller K_{LV} conductances (Kalluri et al., 2010) and may also have larger Na_V conductances open at rest.

To test the impact of Na_V1.6 current in spike timing (Fig. 7), we stimulated firing with frozen trains of synthetically generated ("pseudo") EPSCs with pseudo-random timing to represent the noisy quantal input from hair cells to afferent terminals where spiking normally initiates (Kalluri et al., 2010). In 4 of 14 VGNs tested, block of Na_V1.6 current with 4,9-ah-TTX eliminated EPSC-induced spiking entirely. In the remaining 10 VGNs (6 transient and 4 sustained), we measured regularity with coefficient of variation (CV), avoiding rate-dependent changes in CV by controlling EPSC size to hold spike rate comparable with and without 4,9-ah-TTX (Fig. 7A) (Kalluri et al., 2010). Blocking Na_V1.6 current did not significantly affect CV (Fig. 7B).

In summary, in all firing pattern groups, blocking Na_V1.6 current with 4,9-ah-TTX increased current threshold for spiking and decreased spike rate, spike amplitude and AHP. In sustained VGNs alone, 4,9-ah-TTX also made resting potential appreciably more negative, showing that Na_V1.6 conductance is significant at resting potential. Later (see Fig. S4), we use the computational model to assess the effects of individual current modes on V_{rest}. In a sample of transient and

sustained neurons, blocking $Na_V1.6$ current had no consistent effect on spike regularity when overall rate was held constant by increasing EPSC size.

ATX-II increased excitability and spiking regularity.

In voltage clamp, 100 nM ATX-II, which reduces Na_V channel inactivation, increased Na_VP and Na_VT currents (Fig. 4). We tested its impact on step-evoked firing patterns and pseudo-EPSC-evoked spike trains (Fig. 8).

In a sample of 9 VGNs, ATX-II reduced current threshold to zero and changed step-evoked firing patterns toward more sustained categories in 7 VGNs (3 sustained-A, 2 sustained-C, 2 transient); e.g., sustained-C VGNs became sustained-A (Fig. 8A). ATX-II also increased spike rate and decreased CV in responses to trains of pseudo-EPSCs. To control for rate effects on CV, we decreased EPSC amplitude in ATX-II to match spike rate to the control value (Figure 8C) and still found a consistent, if modest, decrease in CV in ATX-II (Fig. 8C, D). There was no significant effect on AP waveform (Table S4). Figure 8B shows one of 2 of 9 VGNs, both transient, that remained transient, irregular, and relatively inexcitable in ATX-II.

In summary, reducing Na_V channel inactivation with ATX-II lowered current thresholds for both step-and pseudo-EPSC-evoked firing, in most cases to zero current (spontaneous firing). ATX-II also slightly increased spike regularity independent of rate. These results show that ATX-II increases Na_V channel availability near resting potential, presumably by reducing the percentage of inactivated channels, effectively increasing the persistent current.

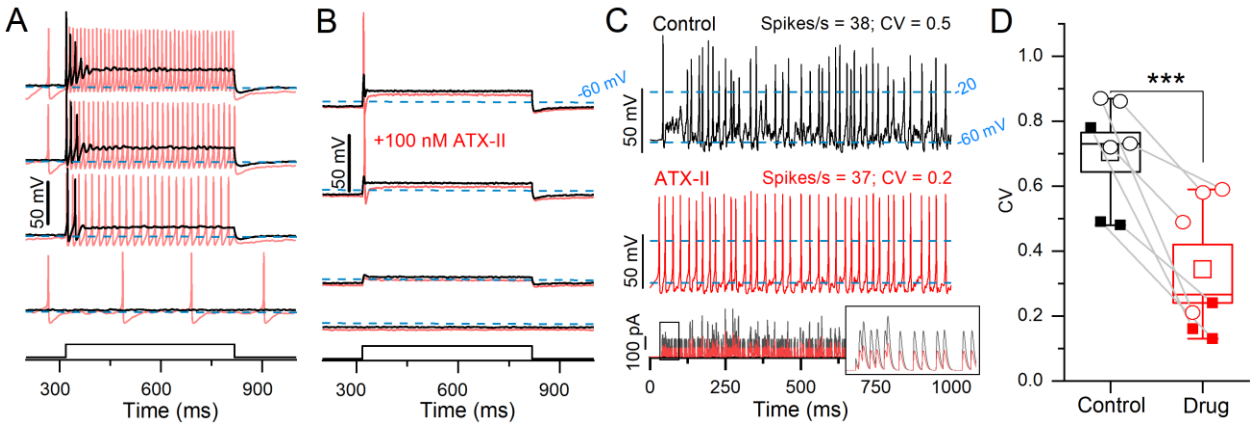

Figure 8 *ATX-II increased spike rate and rate-independent regularity for current steps and EPSC-train stimuli.* **(A)** 100 nm ATX-II (*red*) increased excitability relative to control (*black*) in a P12 sustained-C VGN: increasing the number of APs per step and inducing spontaneous spiking at rest (step current threshold = 0). **(B)** In a P12 transient VGN, current threshold was reduced, but the number of APs remained unchanged. (**C**) Pseudo-EPSC trains (*bottom panel*) evoked spikes in the sustained-C VGN from (A). ATX-II increased spike timing regularity in all VGNs. Inset shows the first 50 ms of EPSC train. To keep spike rate constant between conditions at ~38 spikes/s, smaller EPSCs were applied during ATX-II (*bottom panel*). **(D)** ATX-II decreased CV in every VGN tested (transient = open circles, sustained = filled squares) (0.70 ± 0.06 to 0.34 ± 0.08, paired t-test; n = 7; p = 0.003, Hedges' g = 0.13, small effect).

Modeling the effects of transient, persistent, and resurgent Na_V current on VGN firing

We hypothesized that I-Na_VP and I-Na_VR increase excitability in VGNs by increasing channel availability near spike threshold, and thus enhance the likelihood of firing. Because excitability has been associated with regularity in VGNs, we further hypothesized that I-Na_VP and I-Na_VR enhance regularity independent of rate. Lacking pharmacological tools to disentangle the impacts of Na_VT, Na_VP and Na_VR currents, we adapted existing models of neuronal firing to create model VGNs ("mVGNs") for which each current mode could be adjusted. In the simulations, adding Na_VP and/or Na_VR modes while holding total Na_V current steady had negligible effects on model transient neurons but some effects on model sustained neurons.

We combined a single-compartment conductance-based VGN spiking model (Hight and Kalluri, 2016; Ventura and Kalluri, 2019) with equations for I-Na_VP and I-Na_VR (Wu et al., 2005; Venupogal et al., 2019). The equations for g_{KLV}, g_{KH}, g_H, and g_{leak} were used by Ventura and Kalluri (2019) to describe spiking in rat VGNs. For each mVGN (sustained-A, -B, -C and transient), K_{LV} conductance densities were taken from rat VGN data of multiple sources (Table 2) and ranged from 1.1 mS/cm^2 for transient to 0 for sustained-A. We calculated Na_V conductance density (g_{NaT}) values based on the literature (Table 2) and our data and refined them with model fitting (see Methods): 20 mS/cm^2 for sustained-A, 16 mS/cm^2 for sustained-B, and 13 mS/cm^2 for sustained-C and transient model neurons (Table 3)

We separately simulated four combinations of Na_VT, Na_VP and Na_VR current modes of I-Na_V to assess differential effects on firing: 1) "T", 2) "T + P", 3) "T + R", and 4) "T + P + R". I-Na_VP and I-Na_VR were simulated with conductance density values (expressed as a percentage of g_{NaT}) based on our recordings and separately on larger values obtained from calyx afferent terminal recordings in semi-intact vestibular organs (Meredith & Rennie, 2020) (Methods and Table 3). Current-voltage relations of the simulated currents (dashed curves in Fig. 1D) reproduce the voltage dependence of experimental data.

Another set of simulations explored whether any changes with adding I-Na_VP and I-Na_VR were simply the effect of increasing total Na_V conductance. We increased g_{NaT} ("T+") to match total conductances achieved in other simulations by adding Na_VP and/or Na_VR conductances, and to explore the range of g_{NaT} recorded (Fig. 5B).

Adding I-Na_VR or I-Na_VP reduced refractory periods in response to current steps.

We tested the responses of mVGNs to 500-ms current steps for comparison with step-evoked spike patterns as illustrated for real VGNs in Figure 5A. We show the simulations for I-Na_VP at 2% and I-Na_VR at 10% of I-Na_VT. In Figure 9, we show the first 50 ms of the responses for 5 Na_V combinations: the 4 possible combinations of I-Na_V modes (T, P, R) plus a version (T+) with just I-Na_VT, but increased to match the total conductance density for the (T+P+R) combination.

Adding I-Na_VR affected the firing patterns of sustained-A, -B, and -C mVGNs more than those of transient mVGNs, showing a decrease in the inter-spike interval (ISI). For example, in sustained-A mVGN, ISI decreased in both T+R (44%) and T+P+R (30%) relative to T conditions (Fig. 9A

and Table 6). On its own, I-Na$_V$P decreased ISI slightly (3%). In the sustained-C mVGN, I-Na$_V$R also enhanced the size of oscillations/spikes after the first spike. There was no significant effect in the transient mVGN; I-Na$_V$R enhanced the post-spike voltage oscillation.

Adding I-Na$_V$R or I-Na$_V$P had small effects on firing rates and spike waveforms evoked in model VGNs by current steps.

We tested responses of mVGNs to 500-ms current steps for comparison with step-evoked spike patterns (illustrated for real VGNs in Figure 5A). In Figure 9, we show the first 50 ms of the responses for the 5 I-Na$_V$ combinations, implemented with I-Na$_V$P at 2% of I-Na$_V$T and I-Na$_V$R at

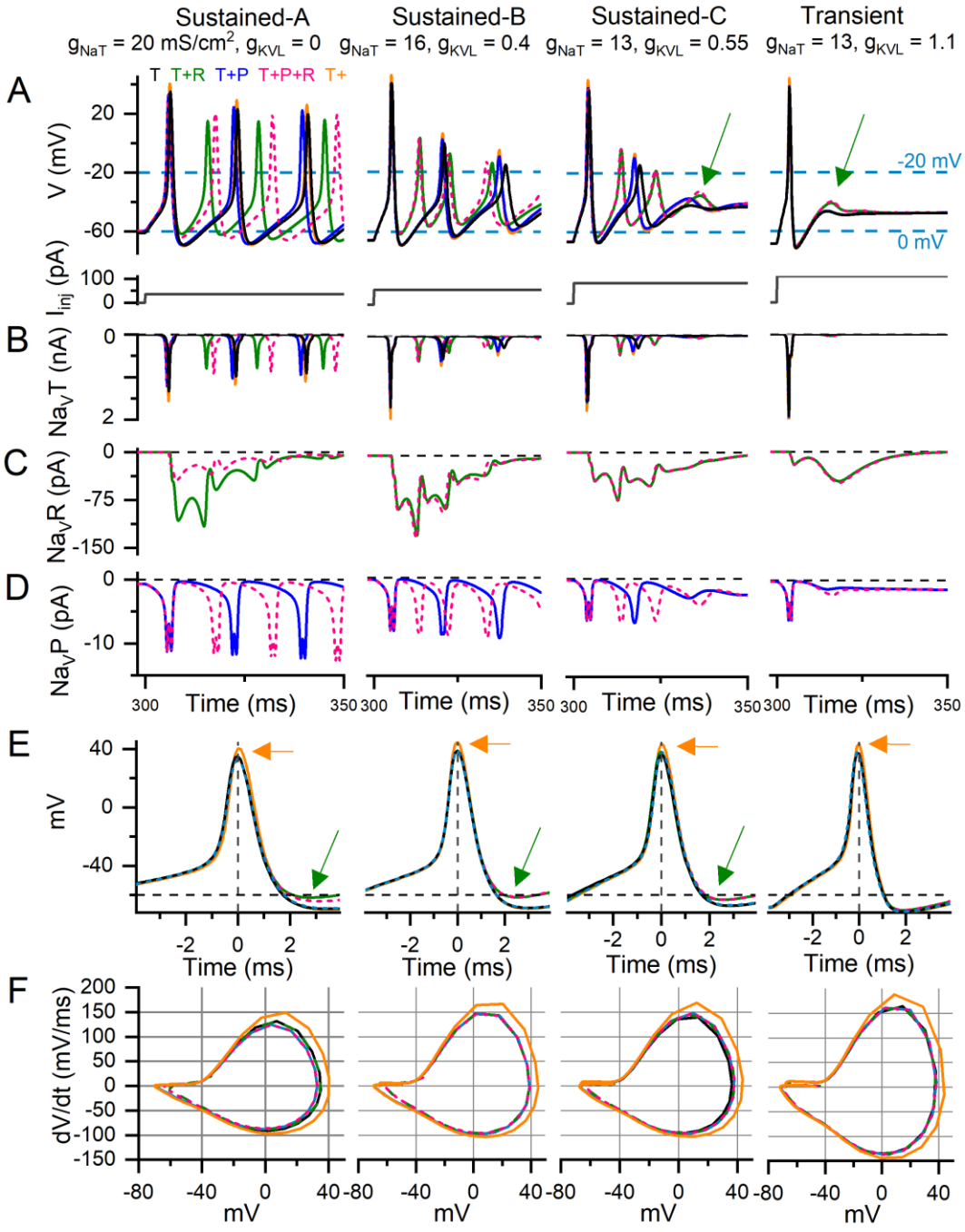

Figure 9 *Adding I-Na$_V$R and I-Na$_V$P altered AP waveform and ISI in current-step responses of sustained model VGNs.* Step-evoked firing in model VGNs with only I-Na$_V$T (T); added I-Na$_V$R (T+R) (10% of I-Na$_V$T); added I-Na$_V$P (T+P) (2% of I-Na$_V$T); both added (T+P+R); and increased I-Na$_V$T (T+). 1st 50 ms of responses to 500-ms current step are shown. Current steps, below, were increased (left to right) to account for increased current thresholds for spiking as firing patterns progressed from sustained-A to transient. Rows B-D show currents corresponding to the above firing pattern and isolated for each current mode (T, R, P). **(A)** In sustained-A, -B, and –C models, adding I-Na$_V$R had variable effects on refractory periods and therefore AP time-to-peak in sustained-A, -B, -C mVGNs, and increased the size of post-spike voltage oscillations in sustained-C and transient mVGNs. Adding I-Na$_V$P slightly decreased refractory periods (time-to-peak) in sustained mVGNs. **(B)** I-Na$_V$T current flow during AP train. To control for increased Na$_V$ conductance with added P and/or R conductance, we also ran a simulation with Na$_V$T conductance density increased by the same amount (22.4, 18, 14.6 mS/cm^2 in sustained-A, -B, -C, transient simulations, respectively; T+ (orange) traces). **(C)** I-Na$_V$R current flow during APs; note that I-Na$_V$R flows during repolarization of each AP and decreases in amplitude with each successive AP in sustained model neurons. **(D)** I-Na$_V$P current flow during AP train; note small variations in peak I-Na$_V$P and the increase in amplitude with each AP in sustained mVGNs. **(E)** Temporally aligning the first APs from trains in (A) shows I-Na$_V$R decreases AHP (green arrows) and increased Na$_V$T increases spike height (orange arrows). **(F)** Phase plane plots show that increasing Na$_V$T also increases peak dV/dt.

10%, based on our mouse VGN data. Small effects of on firing pattern or AP waveform were seen that were not reproduced by simply increasing I-Na$_V$T by the same amount.

Adding I-Na$_V$R and to a lesser extent I-Na$_V$P affected the firing patterns of sustained mVGNs in the direction of increased excitability. As an example, ISI decreased for the sustained-A mVGN in the T+R (44%) and T+P+R (30%) conditions relative to the T-alone condition (Fig. 9A). In sustained-C mVGNs, I-Na$_V$R enhanced the size of spikes and oscillations (green arrow, Fig. 9A) after the first spike. I-Na$_V$P by itself slightly reduced ISI, visibly advancing the third spike in the sustained-A mVGN (3% decrease in ISI).

Adding I-Na$_V$P slightly reduced the spike height and rate of rise for the sustained-A firing pattern (Table 6) but had little effect otherwise. For example, in sustained-A mVGNs, in both T+P and T+P+R condition, adding I-Na$_V$P decreased time-to-peak by 8%, spike height by 4%, spike width by 7%, peak dV/dt by 6%, and increased AHP by 14% (Table 6). There were greater changes seen in the 2nd APs of the trains (e.g., 50% increase in time-to-peak) (Table 6).

Effects of I-Na$_V$R on spike waveform were evident only after a spike had occurred, consistent with its onset during repolarization from the first spike (Fig. 9C) and varied during the spike train. To highlight any effects on spike waveform, Figure 9 (E, F) shows the waveforms and phase-plane plots of aligned first spikes of each mVGN firing pattern shown above. I-Na$_V$R greatly influenced the AHP in the T+R condition, decreasing it by 95%. For example, adding I-Na$_V$R to sustained mVGNs nearly eliminated the first spike's AHP (green arrows, Fig. 9E), but for the sustained-A mVGN, AHP slowly increased with each later spike. and F, Table 6). For transient mVGNs, adding I-Na$_V$R affected the first (and only) spike by enhancing the post-spike oscillation (green arrow, Fig. 9A).

We compared the effects of adding I-Na$_V$R and/or I-Na$_V$P to the effect of adding I-Na$_V$T to the same total conductance (Fig. 9). In current step-evoked firing of sustained-B and -C mVGNs, increasing I-Na$_V$T very slightly decreased ISI after the first spike - demonstrably less than I-Na$_V$R (3% and 8%, respectively) (Fig. 9A, B). Increasing I-Na$_V$T affected first-spike waveforms more

Table 6: AP waveform differences between model VGNs

mVGN (Figure 9)		1st AP:					ISI (ms)	2nd AP:			
	Na_V modes	Time-to-peak (ms)	V_{AP} (mV)	Spike width (ms)	Peak dV/dt (mV/ms)	AHP (mV)		Time-to-peak (ms)	V_{AP} (mV)	Spike width (ms)	Peak dV/dt (mV/ms)
Sustained-A	T	6.3	96.2	1.4	131.7	-8.2	16.9	13.4	84.4	1.9	97.3
	T+P	5.8	92.6	1.3	124.2	-9.4	9.4	12.9	84.3	1.6	100.2
	T+R	6.3	96.2	1.4	131.7	-0.4	16.4	6.6	76.2	1.5	131.7
	T+P+R	5.8	92.6	1.3	124.3	-4.4	11.8	8.7	80.2	1.5	91.5
	T+	6.1	101.7	1.3	149.4	-8.7	16.9	13.4	90.4	1.4	115.4
Sustained-B	T	5.3	104.7	1.2	146.4	-3.1	15.7	12.7	66.8	3	43.5
	T+P	5.2	104.6	1.2	147.6	-3.3	8.4	12.2	67.2	3	48.3
	T+R	5.3	104.7	1.2	146.4	4.2	15.2	5.8	68.5	1.6	146.4
	T+P+R	5.2	104.6	1.2	147.6	4.2	8.2	5.7	68.2	1.6	147.6
	T+	5.2	110.7	1.2	166.6	3.5	15.3	12.2	71	2.4	57.2
Sustained-C	T	4.4	103.0	1.2	139.5	-0.7	14.6	11.8	81.2	3.3	19.5
	T+P	4.1	104.3	1.3	148.1	-0.6	9.5	10.4	76	2.6	27.3
	T+R	4.2	104.6	1.2	145.5	3.3	13.3	6.9	70	2.5	155.2
	T+P+R	4.1	104.3	1.3	148.1	3.2	9.4	6.9	69.5	2.4	148.1
	T+	4.1	110.3	1.3	168.8	-0.8	13.4	10.6	73.4	2.4	32.7
Transient	T	3.6	106.2	1.0	164.6	-3.0					
	T+P	3.6	106.7	1.1	161.3	-3.1					
	T+R	3.6	106.2	1.0	164.6	-1.9					
	T+P+R	3.6	106.7	1.1	161.3	-2.0					
	T+	3.6	112.3	1.0	188.3	-3.3					

Table 6 *AP waveform differences between model VGNs.*

than I-Na_VR or I-Na_VP, substantially increasing spike height and peak rate of rise of first-spike AP waveforms for all firing patterns (compare orange curves with all others, Fig. 9E, F).

In summary, adding I-Na_VR and/or I-Na_VP slightly decreased interspike intervals (thereby increasing instantaneous spike rate) in step-evoked firing of sustained mVGNs. Increasing I-Na_VR reduced AHP. Increasing I-Na_VT had a more substantial effect than I-Na_VR and/or I-Na_VP on spike height and rate of rise.

I-Na_VP made resting potential less negative.

In simulations aiming to reproduce the effects of 4,9-ah-TTX block, we compared step-evoked firing in the sustained-A mVGN and transient mVGN with and without 70% reduction of I-Na_VT (Fig. S4), as observed in real VGNs (Fig. 6). The simulated block increased current thresholds and reduced spike height in both mVGNs and, in the sustained-A mVGN, also reduced spike rate, greatly reduced spike height, and hyperpolarized V_{rest}. These results replicated observations in real VGNs.

We next tested the influence of each Na_V current mode on V_{rest} by simulating the same blocking experiment for different P, R, and T combinations (Fig. S4C). Again, we included I-Na_VP at 2% I-Na_VT, and I-Na_VR at 10% I-Na_VT. V_{rest} has a major influence on excitability by controlling background conductance levels and activation and inactivation states. In these simulations, V_{rest}

was nearly 10 mV more negative for 90% reduced ("blocked") I-Na_VP for the sustained-A mVGN and only 0.5 mV more negative for the transient mVGN. 70% block of Na_VT made V_{rest} ~3 mV more negative in the sustained-A mVGN and had no effect on Vrest in the transient mVGN. 90% reduced I-Na_VR had no effect on V_{rest} in any mVGN, likely because this current is activated during spike repolarization and not at rest.

Therefore, reduction in Na_VT, Na_VP, and Na_VR currents in sustained mVGNs reproduced key effects of 100 nM 4,9-ah-TTX, with I-Na_VP driving the substantial depolarization of V_{rest}.

Effects of I-Na_VT, I-Na_VP or I-Na_VR on simulated spike rate and regularity

To examine the role of Na_V current modes in spike rate and regularity, we drove mVGNs with 1-second trains of simulated synaptic events (pseudo-EPSCs) (Fig. 10A, B), modeled after EPSCs recorded from vestibular afferent calyx events and quasi-randomly distributed in time (see Methods). For each measurement, we used the same set of 5 pseudo-EPSC trains (example is shown in Fig. 10B, bottom trace) and took the mean and SEM of the results.

First, we assessed the effects of I-Na_VT alone on spike rate and spike regularity at 5 values of gNaT density (14 to 22 mS/cm2; Fig. 10B and C; Table S4). For spike rate effects, we generated EPSC trains with inter-event interval and amplitude fixed at 1 ms and 30 pA. Spike rate increased with g_{NaT} density, but leveled off at g_{NaT} = 20 – 22 mS/cm^2 in all mVGNs (Fig. 10A and D, Table S4). For spike regularity effects independent of rate, we kept spike rate approximately constant (~38 spikes/s) across simulations by titrating the size of pseudo-EPSCs while keeping inter-event interval fixed. Increasing I-Na_VT decreased CV in sustained and transient mVGNs, with the effect on Sustained-A not significant (see Table S4 for details).

We then asked whether adding I-Na_VP and/or I-Na_VR influenced spike rate and/or regularity of mVGNs (Fig. 10A, E, and F). For each firing pattern (sustained-A, -B, -C, and transient) and combination of T, P, and R modes, we set g_{NaT} density at 18, 20, and 22 mS/cm^2 and measured spike rate and CV (Fig. 10E, F). We simulated spiking using 2 levels as proportions of I-Na_VT: "VGN" levels (this study: I-Na_VP at 2% of I-Na_VT; I-Na_VR,10%) or at the afferent terminal using "Calyx" levels (I-Na_VP, 4%; I-Na_VR, 20%; Meredith and Rennie, 2020) (Fig. 10A, F, and G; see summary in Table S6). Two-way four factor ANOVAs indicated no interaction in any model VGN between effects of increasing g_{NaT} and the effects of adding Na_V current modes in any mVGN.

Adding I-Na_VP at the lower "VGN" level significantly increased average spike rate only in sustained-C mVGNs. Doubling I-Na_VP to the "Calyx" level enhanced the rate increase in all mVGNs, including the transient mVGN (Fig. 10F). There was no effect of adding just I-Na_VR (T+R condition) on spike rate, but adding I-Na_VR (T+P+R) further increased spike rate over I-Na_VP alone (T+P) for some conditions: VGN-level simulations of sustained mVGNs (medium effect size), and Calyx-level simulations of sustained-C and transient mVGNs (large effect size) (Table S6).

Adding I-Na_VR and/or I-Na_VP affected CV, at a constant spike rate, for some combinations of Na_VT, Na_VP, and Na_VR current modes in sustained mVGNs (Fig. 10F), but these effect sizes were negligible ($g < 0.2$, Table S6). There was no change in transient mVGNs. These simulations suggest that adding I-Na_VP, especially at the 4% level found near spike initiation zones at afferent terminals on hair cells (Meredith and Rennie, 2020), can substantially increase spike rate, even in transient neurons.

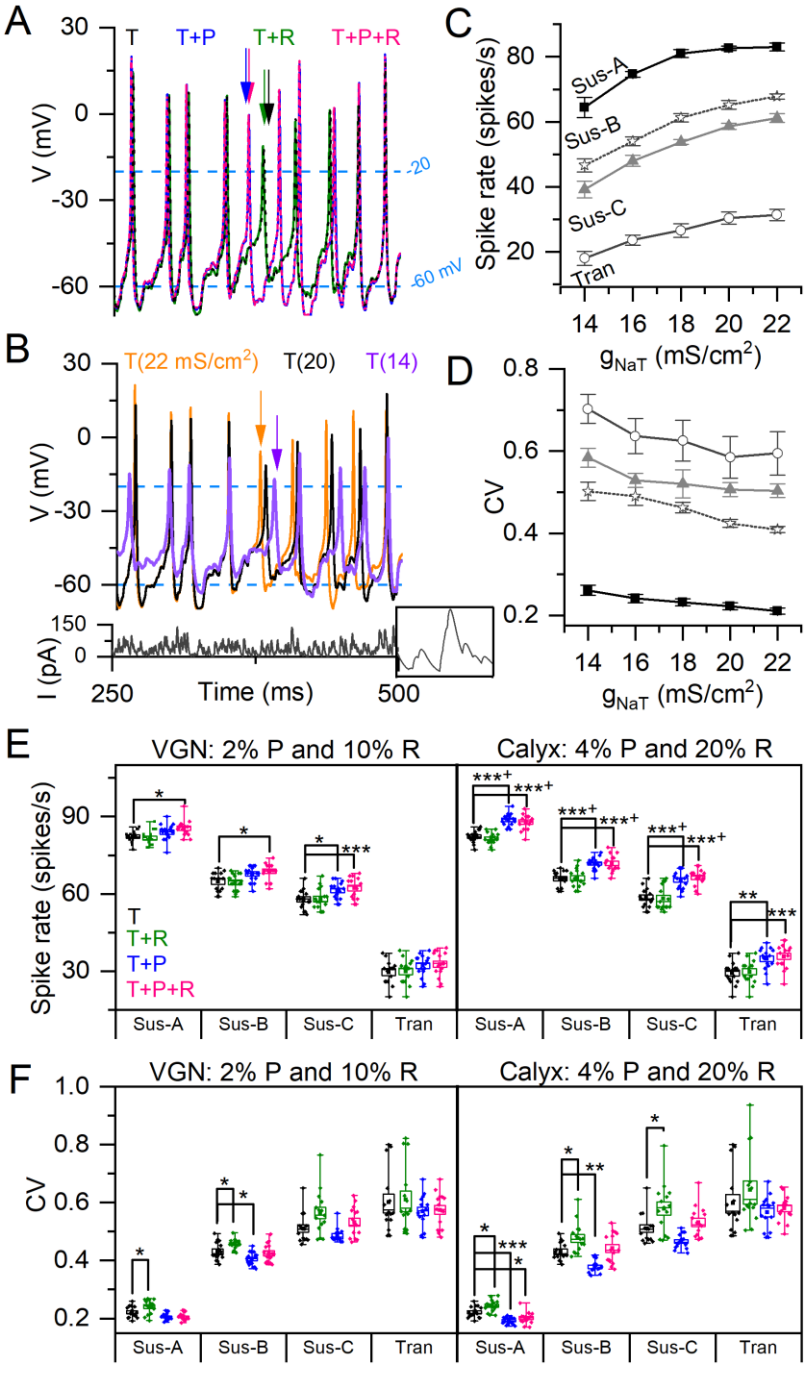

Figure 10 *Adding I-Na_VP increases spike rate in model VGNs.* **(A)** Sustained-A mVGN under different Na_V current combinations, here at "VGN" levels of I-Na_VP (2% of I-Na_VT) and I-Na_VR (10%): adding Na_VP occasionally decreased ISI (see blue and pink arrows) relative to T or T+R (black and green arrows). **(B)** Sustained-A mVGN spike rate for 3 densities of Na_VT: increasing Na_VT can shift spikes and increase spike height (e.g., orange arrow vs. purple arrow). Bottom panel, example of pseudo-EPSC train used to evoke spike trains shown. Inset: 10 ms of EPSCs. **(C)** Increasing Na_VT increased spike rate in all model VGNs but plateaued above 18 mS/cm^2. **(D)** Increasing Na_VT decreased CV in all model VGNs and again, roughly plateaued after 18 mS/cm2. **(E)** Summary of spike rates from 15simulations for each combination of Na_V current modes and firing pattern, including Na_VT from (C) and comparing multiple NaV components conditions. T+P+R and T+P conditions showed increased spike rate relative to Na_VT in sustained-A, -B, and –C mVGN in VGN conductances level simulations (2% and 10%), and all mVGNs in calyx simulations (4% and 20%). Na_VR has no effect on spike rate. **(F)** A summary of CV at ~38 spikes/s, including I-Na_VT from (D) and comparing multiple Na_V components. Differences are highly significant but in each case the effect size was very small (Table S6).

DISCUSSION

VGNs as a model preparation for firing patterns in the vestibular nerve

VGNs are cell bodies that, when mature and *in vivo*, are bipolar, inter-nodal and myelinated. Research from multiple groups (Chabbert et al., 1997; Limon et al., 2005; Iwasaki et al., 2008) has shown that isolated VGNs express voltage-gated currents and firing patterns that resemble currents and firing at spike initiation zones just below the hair cell-afferent terminal synapses in the vestibular epithelium, as illustrated by immunohistochemistry and direct recordings from calyx terminals (e.g., Lysakowski et al., 2011; Songer and Eatock, 2013; Meredith and Rennie, 2020). It is not clear whether the presence of these channels in the dissociated cell bodies represents true somatic expression, or whether nodal Na_V channels and paranodal K_V channels on either side of the soma come along during dissociation. In most cases, investigators have cultured the dissociated VGNs overnight, causing the VGNs to shed their myelin and expose the neural membrane for whole-cell patch recording.

In rat VGNs, there is some evidence that overnight culturing eliminates expression of some types of pore-forming Na_V channels. Dissociated young rat VGNs that were studied acutely had multiple transient Na_V currents with distinct voltage dependence and TTX sensitivity (Liu et al., 2016), including an $Na_V1.5$ current (negatively shifted voltage range, TTX-insensitive) and an $Na_V1.8$ current (positively shifted voltage range, TTX-resistant). These non-TTX-sensitive forms were not detected in overnight-cultured rat VGNs (Liu et al., 2016). Age differences across studies may also matter. $Na_V1.5$ expression in ganglion cell bodies may be an immature feature, as suggested by its time course of expression in small rat DRG neurons (Ranganathan et al. 2002) and some decline in current expression over the first postnatal week in rat VGNs (Liu et al. 2016). Meredith and Rennie (2020) recorded TTX-insensitive currents (consistent with $Na_V1.5$) from gerbil afferent calyceal terminals, and but only in afferents younger than P12.

Thus, isolated and cultured VGNs are compact cell bodies that allow high-quality voltage clamp recordings and reproduce some but not all naturally occurring ion channel expression. Importantly for our purposes, they show a range of firing patterns consistent with a role for intrinsic neuronal properties in setting up the different encoding strategies (temporal vs. rate) characteristic of irregular and regular afferent populations (Jamali et al., 2016; Cullen, 2019). Previous work has documented the difference in firing patterns of VGNs and probed their relationship to specific ion channels: low-voltage-activated K_V1 (Iwasaki et al., 2008) and K_V7 channels (Kalluri et al., 2010), $Ca2^+$-dependent K channels (Limon et al. 2005), HCN channels (Horwitz et al., 2014) and Na_V channels (Liu et al. 2016). By going beyond correlation and developing a method to interrogate regularity in these synapse-less somata, a particularly strong case was made for K_{LV} channels (Kalluri et al., 2010). We took this approach with Na_V channel modes and provide support for a substantial role of relatively small persistent and resurgent currents in excitability and related properties such as resting potential.

$Na_V1.6$ is the major Na_V subunit in VGNs, contributing to resting potential and excitability

All VGNs in our sample expressed I-Na_VT and about half also expressed I-Na_VP, with no clear change in incidence with age (range P3-28), in contrast to mouse cochlear ganglion neurons, where

both persistent and resurgent forms increased with maturation (Browne et al., 2017). We saw no I-Na_VR before P10. Beyond P10, the incidence was 12% (6/49 tested). VGNs also have voltage-dependent Ca^{2+} (Ca_V) currents (L-, N-, P/Q-, R-, and T-type) (Desmadryl et al. 1997; Chambard et al. 1999) which drive Ca^{2+}-dependent K^+ currents that reduce sustained firing (Limón et al., 2005). Here we suppressed both Ca_V and Ca^{2+}-dependent K^+ currents by eliminating all but trace Ca^{2+} from the external medium. Our experiments do not indicate whether sustained VGNs have more Na_VP or Na_VR current than transient neurons, but modeling suggests that in transient neurons, Na_VP and Na_VR currents, if present, would have little effect on rate, regularity and resting potential.

RT-PCR of whole rat vestibular ganglia indicated expression of most Na_V pore-forming (α) subunits and all auxiliary (β) subunits (Liu et al. 2016). Block by the $Na_V1.6$-selective blocker, 4,9-ah-TTX, however, indicates that $Na_V1.6$ channels make up much or all of the current we recorded, for all modes, again consistent with results from calyx terminals in gerbil cristae (Meredith and Rennie, 2020). In our study, 100 nM 4,9-ah-TTX blocked Na_VT current by a similar amount (~50%) in sustained and transient firing VGNs, suggesting that they express similar densities of $Na_V1.6$ channels. Persistent and resurgent I-Na_V were almost fully blocked. Cochlear spiral ganglion neurons also express 4,9-ah-TTX-sensitive transient, persistent, and resurgent currents (Browne et al. 2017), and are immunoreactive for $Na_V1.6$ at spike initiation zones next to their terminals on hair cells (Kim and Rutherford, 2016). I-Na_VR is theorized to arise from the internal block of Na_V channels, canonically $Na_V1.6$, by a positively charged molecule, e.g., Na_V auxiliary subunit β4 or fibroblast growth factor homologous factor 14 (Raman and Lewis, 2014; White et al., 2019).

The residual Na_V current in 4,9-ah-TTX had significantly more negative inactivation than the control and blocked currents, but not nearly as negative as the TTX-insensitive current carried by $Na_V1.5$ in acutely cultured, immature rat VGNs (Liu et al., 2016). The RT-PCR data from rat vestibular ganglia (Liu et al., 2016) suggest $Na_V1.1$, 1.2, 1.3, and 1.7 as candidates.

As expected for a major Na_V current, the $Na_V1.6$ currents are critical to excitability in both firing types. In both sustained and transient neurons, spikes were substantially smaller in 4,9-ah-TTX, as expected from the strong block of the dominant transient mode $Na_V1.6$ current. A large decrease in AHP size presumably reflected both the small spike height (reducing activation of K^+ currents that cause AHPs) and the more negative V_{rest} (reducing the voltage difference from E_K). 4,9-ah-TTX blocking experiments showed that $Na_V1.6$ channels contribute to resting potential in sustained neurons (Fig. 6I; Table S4).

Our modeling also suggests that Na_VP and, to a lesser extent, Na_VT current modes may significantly contribute to resting conductance in sustained VGNs (Fig. S4). Although I-Na_VP contributed just 2% of maximum Na_V current density in VGNs, Na_VP current at resting potential may be closer to 10% of total current, based on its relative voltage dependence and the substantial (~30%) steady-state inactivation of Na_VT current even at resting potential (Fig. 2B). The small to negligible effect of blocking $Na_V1.6$ channels on resting potential in transient VGNs (Fig. 6J vs. 6I) is consistent with resting conductance being dominated by their greater density of K_{LV}

channels. HCN conductances may also contribute to resting membrane potential in VGNs, depending on the balance of resting conductances (Ventura and Kalluri, 2019).

Effects of Na_V current modes on AP waveforms and firing patterns

AP height and rate of rise varied across firing pattern (Fig. 5C ,F) and correlated modestly with maximum Na_V conductance density (Fig. 5D), both for all VGNs and for transient VGNs alone, which showed the greatest variance in maximum Na_V conductance density. VGNs with different firing patterns, in contrast, did not have significantly different Na_V G_{max} density. G_{max} density is dominated by the Na_VT current mode, so these correlations do not reveal roles for I-Na_VP, which has a more significant effect near resting potential, and I-Na_VR, which acts during spike repolarization. To isolate their effects, we used simulations.

In sustained model VGNs, I-Na_VP had a stronger effect than other modes on resting potential, depolarizing V_{rest} by ~10 mV. The effect on V_{rest}, in turn, shapes many AP metrics by affecting resting (input) conductance, inactivation state of I-Na_VT, and current and voltage thresholds for spikes. I-Na_VP reduced time-to-peak in sustained mVGNs' APs and made transient APs wider. I-Na_VP also significantly increased firing rate, with a medium effect size for the 2% of transient current that we found in VGNs and a very large effect size for the 4% value based on published recordings (Meredith and Rennie, 2020) from calyceal terminals (Table S6). At either 2% or 4%, persistent current had negligible effect (Hedge's $g \leq 0.02$) on regularity (CV) (as measured with constant spike rate).

In current step simulations (Fig. 9A, B), adding I-Na_VR altered instantaneous spike rate in sustained mVGNs by truncating the AHP, decreasing the current threshold for spiking, and shortening ISI between the first two spikes. However, when tested with trains of pseudo-EPSCs, I-Na_VR had no significant effect on average spike rate across multiple spike trains (Table S6), suggesting that long term effects of resurgent current reduce the impact of short-term changes in rate. Although in some simulated cases, resurgent current affected regularity (CV) independent of spike rate, the effects were very small (Hedge's $g \leq 0.02$; Table S6). Thus, under the conditions of our simulations, I-Na_VR had little effect on the key properties that distinguish vestibular afferents, rate and regularity.

Our simulations support previous work indicating a dominant role for K_{LV} currents in differentiating spike rate and regularity of sustained (presumed regular) and transient (presumed irregular) VGNs (Kalluri et al., 2010; Ventura and Kalluri, 2019). *In vivo,* many factors differ across the peripheral and central epithelial zones that give rise to regular and irregular afferents, including the nature of the mechanical input to hair cells, numbers and types of synaptic inputs, relative contributions of non-quantal and quantal transmission, size of dendritic arbors, and complement of expressed ion channels, all of which might contribute to voltage noise at spike initiation zones. K_{LV} currents increase irregularity by enhancing the afferent's sensitivity to high-frequency noise (Kalluri et al., 2010). In transient VGNs, K_{LV} currents are larger, limiting the effects of varying Na_V current modes on rate and regularity. For sustained VGNs with small K_{LV} currents, increasing I-Na_VT and I-Na_VP increases spike rate, which, *in vivo,* will naturally increase regularity.

Conflict of Interest

The authors declare that the research was conducted in the absence of any commercial or financial relationships that could be construed as a potential conflict of interest.

Author Contributions

SBL conceived the project, planned and performed the electrophysiological recordings and computational modeling, and wrote the first draft of the manuscript. RAE participated in planning, design, analysis, and writing the manuscript.

Funding

This study was supported by the National Institutes of Health (R01 DC012347), awarded to RAE, and the Howard Hughes Medical Institute Gilliam Fellowship for Advanced Study, awarded to SBL

Acknowledgments

We are grateful to Dr. Omar López-Ramírez for sharing excitatory postsynaptic current data from vestibular afferent terminals and to Dr. Radha Kalluri for access to the original VGN spiking model. We thank Hannah Martin, Dr. Aravind Govindaraju, and Dr. Kalluri for comments on early versions of the manuscript.

References

Alexander SPH, **Mathie A**, **Peters JA**, **Veale EL**, **Striessnig J**, **Kelly E**, **Armstrong JF**, **Faccenda E**, **Harding SD**, **Pawson AJ**, **Southan C**, **Davies JA**, **Aldrich RW**, **Attali B**, **Baggetta AM**, **Becirovic E**, **Biel M**, **Bill RM**, **Catterall WA**, **Conner AC**, **Davies P**, **Delling M**, **Virgilio FD**, **Falzoni S**, **Fenske S**, **George C**, **Goldstein SAN**, **Grissmer S**, **Ha K**, **Hammelmann V**, **Hanukoglu I**, **Jarvis M**, **Jensen AA**, **Kaczmarek LK**, **Kellenberger S**, **Kennedy C**, **King B**, **Kitchen P**, **Lynch JW**, **Perez-Reyes E**, **Plant LD**, **Rash L**, **Ren D**, **Salman MM**, **Sivilotti LG**, **Smart TG**, **Snutch TP**, **Tian J**, **Trimmer JS**, **Van den Eynde C**, **Vriens J**, **Wei AD**, **Winn BT**, **Wulff H**, **Xu H**, **Yue L**, **Zhang X**, **Zhu M**. THE CONCISE GUIDE TO PHARMACOLOGY 2021/22: Ion channels. *British Journal of Pharmacology* 178: S157–S245, 2021.

Bant JS, **Raman IM**. Control of transient, resurgent, and persistent current by open-channel block by Na channel β4 in cultured cerebellar granule neurons. *Proceedings of the National Academy of Sciences* 107: 12357–12362, 2010.

Bean BP. The action potential in mammalian central neurons. *Nature Reviews Neuroscience* 8: 451–465, 2007.

Brown AM, **Schwindt PC**, **Crill WE**. Different voltage dependence of transient and persistent Na+ currents is compatible with modal-gating hypothesis for sodium channels. *Journal of Neurophysiology* 71: 2562–2565, 1994.

Browne L, **Smith KE**, **Jagger DJ**. Identification of Persistent and Resurgent Sodium Currents in Spiral Ganglion Neurons Cultured from the Mouse Cochlea. *eNeuro* ENEURO.0303-17.2017, 2017.

Chabbert C, **Chambard J-M**, **Valmier J**, **Sans A**, **Desmadryl G**. Voltage-activated sodium currents in acutely isolated mouse vestibular ganglion neurones. *NeuroReport* 8: 1253, 1997.

Chambard JM, **Chabbert C**, **Sans A**, **Desmadryl G**. Developmental changes in low and high voltage-activated calcium currents in acutely isolated mouse vestibular neurons. *The Journal of Physiology* 518: 141–149, 1999.

Crill WE. Persistent Sodium Current in Mammalian Central Neurons. *Annual Review of Physiology* 58: 349–362, 1996.

Cullen KE. Vestibular processing during natural self-motion: implications for perception and action. *Nat Rev Neurosci* 20: 346–363, 2019.

Denomme N, **Lukowski AL**, **Hull JM**, **Jameson MB**, **Bouza AA**, **Narayan ARH**, **Isom LL**. The voltage-gated sodium channel inhibitor, 4,9-anhydrotetrodotoxin, blocks human Nav1.1 in addition to Nav1.6. *Neuroscience Letters* 724: 134853, 2020.

Desmadryl G, **Chambard J-M**, **Valmier J**, **Sans A**. Multiple voltage-dependent calcium currents in acutely isolated mouse vestibular neurons. *Neuroscience* 78: 511–522, 1997.

Do, MTH., Bean BP. Subthreshold sodium currents and pacemaking of subthalamic neurons: modulation by slow inactivation. *Neuron* 39.1: 109-120, 2003.

Do MTH, **Bean BP**. Sodium Currents in Subthalamic Nucleus Neurons From Nav1.6-Null Mice. *Journal of Neurophysiology* 92: 726–733, 2004.

Durlak JA. How to Select, Calculate, and Interpret Effect Sizes. *Journal of Pediatric Psychology* 34: 917–928, 2009.

Eatock RA, **Xue J**, **Kalluri R**. Ion channels in mammalian vestibular afferents may set regularity of firing. *Journal of Experimental Biology* 211: 1764–1774, 2008.

Gentet LJ, **Stuart GJ**, **Clements JD**. Direct Measurement of Specific Membrane Capacitance in Neurons. *Biophysical Journal* 79: 314–320, 2000.

Gittis AH, **Moghadam SH**, **du Lac S**. Mechanisms of Sustained High Firing Rates in Two Classes of Vestibular Nucleus Neurons: Differential Contributions of Resurgent Na, Kv3, and BK Currents. *Journal of Neurophysiology* 104: 1625–1634, 2010.

Goldberg JM. Afferent diversity and the organization of central vestibular pathways. *Exp Brain Res* 130: 277–297, 2000.

Hight AE, **Kalluri R**. A biophysical model examining the role of low-voltage-activated potassium currents in shaping the responses of vestibular ganglion neurons. *Journal of Neurophysiology* 116: 503–521, 2016.

Hodgkin AL, **Huxley AF**. A quantitative description of membrane current and its application to conduction and excitation in nerve. *The Journal of Physiology* 117: 500–544, 1952.

Holmes WR, **Huwe JA**, **Rowe MH**, **Peterson EH**. Afferent-hair cell connectivity as a possible source of spike train irregularity in turtle vestibular bouton afferents. *BMC Neuroscience* 15: P69, 2014.

Hong H, **Lu T**, **Wang X**, **Wang Y**, **Sanchez JT**. Resurgent sodium current promotes action potential firing in the avian auditory brainstem. *The Journal of Physiology* 596: 423–443, 2018.

Horwitz, GC, Risner-Janiczek JR, and Holt JR. Mechanotransduction and hyperpolarization-activated currents contribute to spontaneous activity in mouse vestibular ganglion neurons. *Journal of General Physiology* 143.4 (2014): 481-497.

Iwasaki S, **Chihara Y**, **Komuta Y**, **Ito K**, **Sahara Y**. Low-Voltage-Activated Potassium Channels Underlie the Regulation of Intrinsic Firing Properties of Rat Vestibular Ganglion Cells. *Journal of Neurophysiology* 100: 2192–2204, 2008.

Jamali M, **Chacron MJ**, **Cullen KE**. Self-motion evokes precise spike timing in the primate vestibular system. *Nature Communications* 7: 13229, 2016.

Kalluri R, **Xue J**, **Eatock RA**. Ion Channels Set Spike Timing Regularity of Mammalian Vestibular Afferent Neurons. *Journal of Neurophysiology* 104: 2034–2051, 2010.

Kay AR, **Sugimori M**, **Llinás R**. Kinetic and Stochastic Properties of a Persistent Sodium Current in Mature Guinea Pig Cerebellar Purkinje Cells. *Journal of Neurophysiology* 80: 1167–1179, 1998.

Khaliq ZM, **Gouwens NW**, **Raman IM**. The Contribution of Resurgent Sodium Current to High-Frequency Firing in Purkinje Neurons: An Experimental and Modeling Study. *J Neurosci* 23: 4899–4912, 2003.

Kim KX, **Rutherford MA**. Maturation of NaV and KV Channel Topographies in the Auditory Nerve Spike Initiator before and after Developmental Onset of Hearing Function. *J Neurosci* 36: 2111–2118, 2016.

Klinger AB, **Eberhardt M**, **Link AS**, **Namer B**, **Kutsche LK**, **Schuy ET**, **Sittl R**, **Hoffmann T**, **Alzheimer C**, **Huth T**, **Carr RW**, **Lampert A**. Sea-Anemone Toxin ATX-II Elicits A-Fiber-Dependent Pain and Enhances Resurgent and Persistent Sodium Currents in Large Sensory Neurons. *Mol Pain* 8: 1744-8069-8–69, 2012.

Lewis AH, **Raman IM**. Resurgent current of voltage-gated Na+ channels. *The Journal of Physiology* 592: 4825–4838, 2014.

Limón A, **Pérez C**, **Vega R**, **Soto E**. Ca2+-Activated K+-Current Density Is Correlated With Soma Size in Rat Vestibular-Afferent Neurons in Culture. *Journal of Neurophysiology* 94: 3751–3761, 2005.

Liu X-P, **Wooltorton JRA**, **Gaboyard-Niay S**, **Yang F-C**, **Lysakowski A**, **Eatock RA**. Sodium channel diversity in the vestibular ganglion: NaV1.5, NaV1.8, and tetrodotoxin-sensitive currents. *Journal of Neurophysiology* 115: 2536–2555, 2016.

Lysakowski A, **Gaboyard-Niay S**, **Calin-Jageman I**, **Chatlani S**, **Price SD**, **Eatock RA**. Molecular Microdomains in a Sensory Terminal, the Vestibular Calyx Ending. *J Neurosci* 31: 10101–10114, 2011.

Meredith FL, **Rennie KJ**. Zonal variations in K+ currents in vestibular crista calyx terminals. *Journal of Neurophysiology* 113: 264–276, 2015.

Meredith FL, **Rennie KJ**. Regional and Developmental Differences in Na+ Currents in Vestibular Primary Afferent Neurons. *Front Cell Neurosci* 12, 2018.

Meredith FL, **Rennie KJ**. Persistent and resurgent Na+ currents in vestibular calyx afferents. *Journal of Neurophysiology* 124: 510–524, 2020.

Oliveira JS, **Redaelli E**, **Zaharenko AJ**, **Cassulini RR**, **Konno K**, **Pimenta DC**, **Freitas JC**, **Clare JJ**, **Wanke E**. Binding Specificity of Sea Anemone Toxins to Nav 1.1-1.6 Sodium Channels: UNEXPECTED CONTRIBUTIONS FROM DIFFERENCES IN THE IV/S3-S4 OUTER LOOP *. *Journal of Biological Chemistry* 279: 33323–33335, 2004.

Patel RR, **Barbosa C**, **Xiao Y**, **Cummins TR**. Human Nav1.6 Channels Generate Larger Resurgent Currents than Human Nav1.1 Channels, but the Navβ4 Peptide Does Not Protect Either Isoform from Use-Dependent Reduction. *PLOS ONE* 10: e0133485, 2015.

Raman IM, **Bean BP**. Resurgent Sodium Current and Action Potential Formation in Dissociated Cerebellar Purkinje Neurons. *J Neurosci* 17: 4517–4526, 1997.

Raman IM, **Sprunger LK**, **Meisler MH**, **Bean BP**. Altered subthreshold sodium currents and disrupted firing patterns in Purkinje neurons of Scn8a mutant mice. *Neuron* 19: 881–891, 1997.

Renganathan M, **Dib-Hajj S**, **Waxman SG**. Nav1.5 underlies the 'third TTX-R sodium current' in rat small DRG neurons. *Molecular Brain Research* 106: 70–82, 2002.

Risner JR, **Holt JR**. Heterogeneous Potassium Conductances Contribute to the Diverse Firing Properties of Postnatal Mouse Vestibular Ganglion Neurons. *J Neurophysiol* 96: 2364–2376, 2006.

Rosker C, **Lohberger B**, **Hofer D**, **Steinecker B**, **Quasthoff S**, **Schreibmayer W**. The TTX metabolite 4,9-anhydro-TTX is a highly specific blocker of the Nav1.6 voltage-dependent sodium channel. *American Journal of Physiology-Cell Physiology* 293: C783–C789, 2007.

Rothman JS, **Manis PB**. The Roles Potassium Currents Play in Regulating the Electrical Activity of Ventral Cochlear Nucleus Neurons. *Journal of Neurophysiology* 89: 3097–3113, 2003.

Songer JE, **Eatock RA**. Tuning and Timing in Mammalian Type I Hair Cells and Calyceal Synapses. *J Neurosci* 33: 3706–3724, 2013.

Stafstrom CE, **Schwindt PC**, **Crill WE**. Negative slope conductance due to a persistent subthreshold sodium current in cat neocortical neurons in vitro. *Brain Research* 236: 221–226, 1982.

Ventura CM, **Kalluri R**. Enhanced Activation of HCN Channels Reduces Excitability and Spike-Timing Regularity in Maturing Vestibular Afferent Neurons. *J Neurosci* 39: 2860–2876, 2019.

Venugopal S, **Seki S**, **Terman DH**, **Pantazis A**, **Olcese R**, **Wiedau-Pazos M**, **Chandler SH**. Resurgent Na+ Current Offers Noise Modulation in Bursting Neurons. *PLOS Computational Biology* 15: e1007154, 2019.

Wanke E, **Zaharenko AJ**, **Redaelli E**, **Schiavon E**. Actions of sea anemone type 1 neurotoxins on voltage-gated sodium channel isoforms. *Toxicon* 54: 1102–1111, 2009.

White HV, **Brown ST**, **Bozza TC**, **Raman IM**. Effects of FGF14 and NaVβ4 deletion on transient and resurgent Na current in cerebellar Purkinje neurons. *Journal of General Physiology* 151: 1300–1318, 2019.

Wu N, **Enomoto A**, **Tanaka S**, **Hsiao C-F**, **Nykamp DQ**, **Izhikevich E**, **Chandler SH**. Persistent Sodium Currents in Mesencephalic V Neurons Participate in Burst Generation and Control of Membrane Excitability. *Journal of Neurophysiology* 93: 2710–2722, 2005.

Data Availability Statement

The associated code is accessible in the following repository: https://github.com/eatocklab/NaV-currents-in-VGN-spiking.

The datasets generated and analyzed for both electrophysiology and modeling experiments can be found in our Dryad repository: https://doi.org/10.5061/dryad.k3j9kd5f7 (forthcoming).

894 # Supplementary Figures

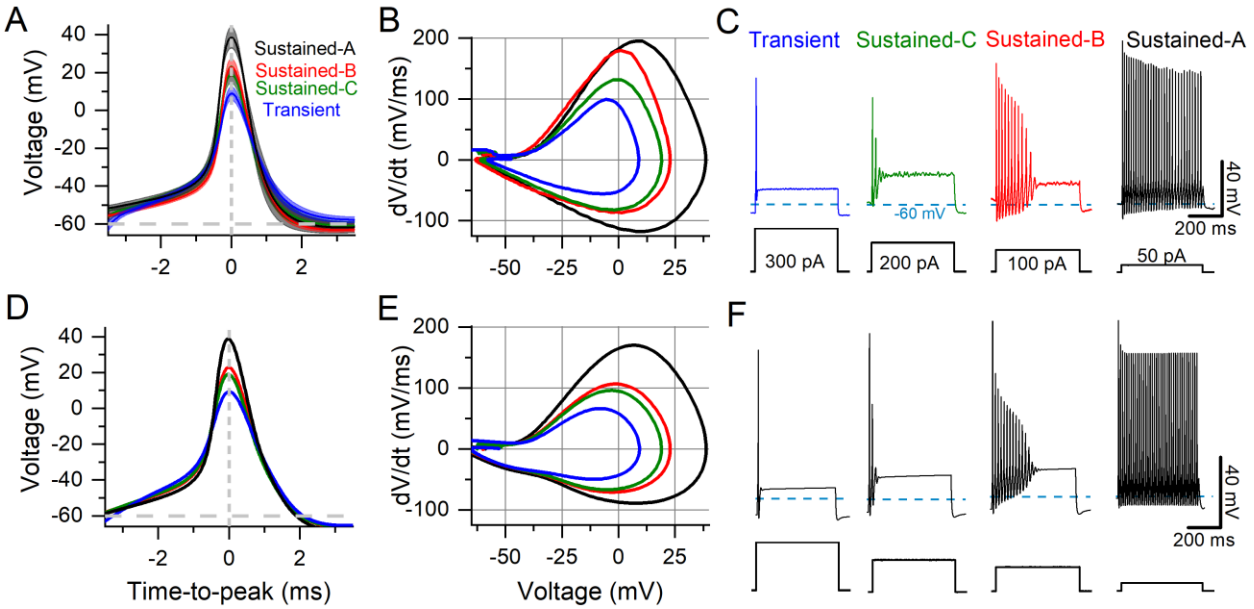

Figure S1 *Comparison of VGN responses to model VGN simulations.* **(A – C)** (reproduced from Fig. 5). Averaged recorded APs (A), corresponding mean phase-plane plots (B), and exemplar step-evoked firing patterns (C). **(D)** Model-generated APs based on APs from A. **(E)** Phase-plane plots for simulated APs from (D)**.** Simulated APs have smaller peak rates of depolarization. **(F)** Step-evoked firing patterns of model VGNs capture key features of exemplar data in (C).

895

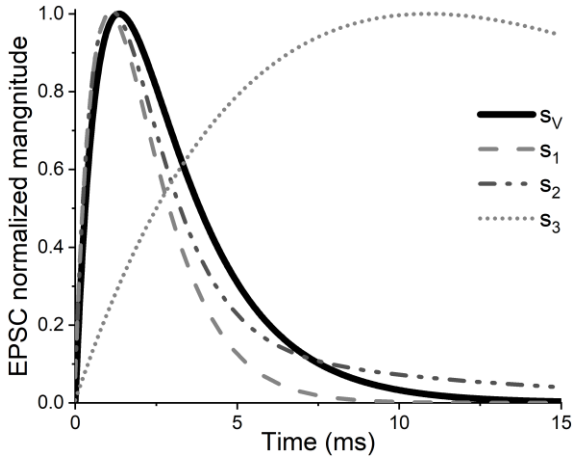

Figure S2 *Shape of simulated EPSCs.* Simulated excitatory postsynaptic currents (EPSCs) used to evoke spiking in our cell-autonomous model were modeled after spontaneous vestibular synaptic potentials (s_V) recorded at room temperature in mouse calyces. EPSC shapes previously tested in Hight and Kalluri (2016) (s1, s2, and s3) are shown for comparison.

896

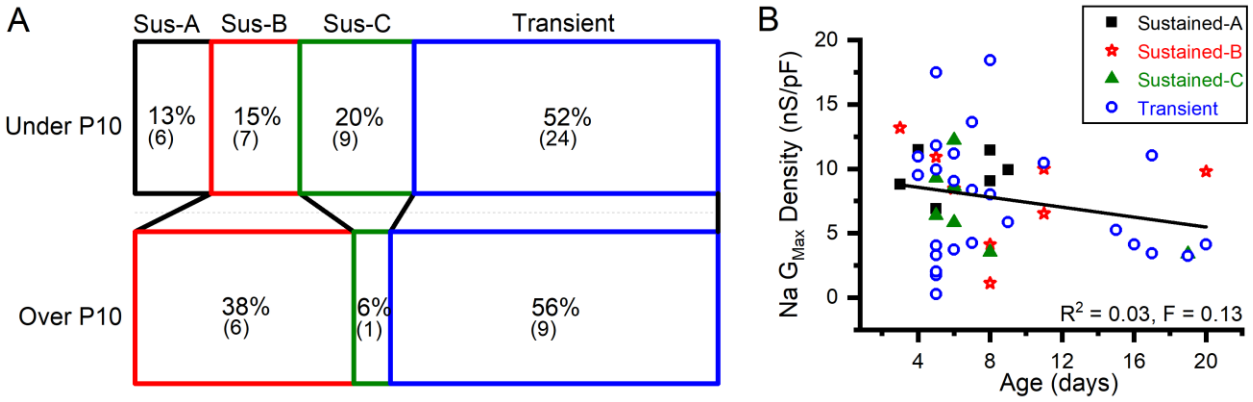

Figure S3 *Changes in firing patterns and Na_V conductance density with age.* (**A**) Change in distribution of firing pattern in younger and older VGNs. (**B**) No relationship between Na_V G_{max} Density and postnatal age.

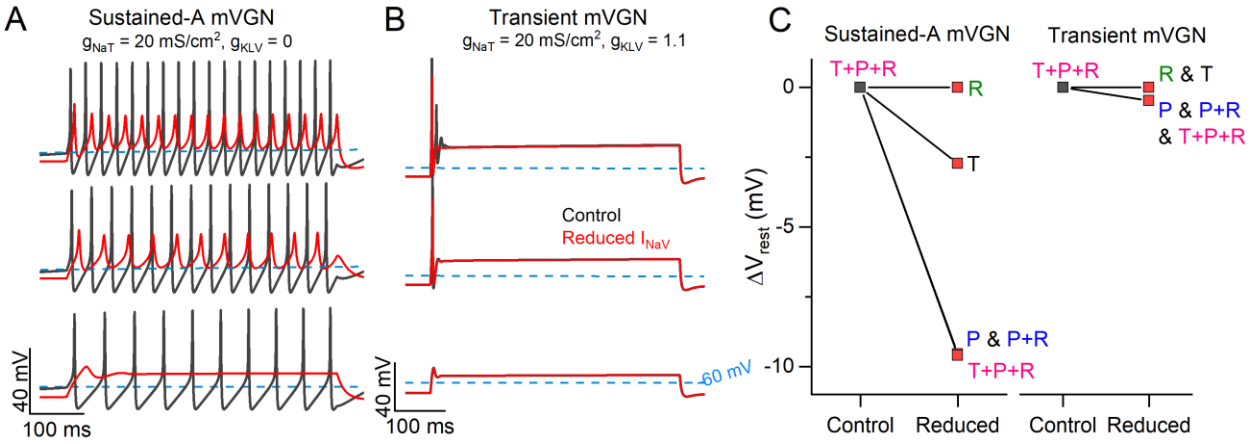

Figure S4 *Reducing Na_V current modes replicates 4,9-ah-TTX block in model sustained and transient VGNs.* **(A & B)** Firing patterns for a sustained-A (A) and transient (B) mVGNs with (black) control Na_V densities of 20 mS/cm^2. Reducing (red) I-Na_VT by 70% replicates results observed with application of 4,9-ah-TTX in sustained-A mVGNs: increase in current threshold, reduction inreduced spike height and spike rate, and slight hyperpolarization in V_{rest}. **(B)** Transient mVGNs had reduced in spike height. **(C)** Na_VP and Na_VT drives hyperpolarization in sustained mVGNs. Each individual component was reduced by the estimated 4,9-ah-TTX block percentage: Na_VR and Na_VP were each reduced by 90% and Na_VT by 70%. Reducing ("blocking") each individual component and combinations of components at a time shows that blocking Na_VT and Na_VP hyperpolarizes resting membrane potential.

Supplementary Tables

Table S1: Summary of one-way ANOVA tests for voltage clamp experiments

Na_V conductance density (Fig 2B)		F(2,70) = 6.7, p = 0.002, power = 0.90	
		p	effect size, interpretation
	Na_VT vs Na_VT+P	0.33	
	Na_VT vs Na_VT+P+R	0.002	0.27, small
	Na_VT+P vs Na_VT+P+R	0.02	0.41, med
		Activation, $V_{1/2}$	**Inactivation, $V_{1/2}$**
Na_V current modes (Fig 2C)		F(2,27) = 5.9, p = 0.008, power = 0.83	F(2,26) = 0.38, p = 0.68, power = 0.10
	Bonferroni test:	p / effect size	p
	Na_VT vs Na_VT+P	1	0.66
	Na_VT vs Na_VT+P+R	0.009 / 0.75, big	0.86
	Na_VT+P vs Na_VT+P+R	0.02 / 0.59, med	0.97
4,9-ah-TTX (Fig 3B)	(n = 12)	F(2, 35) = 1.1, p = 0.35, power = 0.22	F(2, 35) = 5.5, p = 0.009, power = 0.82
	Bonferroni test:	p	p / effect size
	Control vs Residual	0.52	0.02 / 0.69, med
	Control vs Blocked	1	1
	Residual vs Blocked	0.83	0.02 / 0.66, med
ATX-II (Fig 4)	(n = 7)	**Activation, $V_{1/2}$**	**Inactivation, $V_{1/2}$**
	Paired t-test:	p / power	p / power
	Na_VT: Control vs ATX-II	0.34 / 0.13	0.06 / 0.48
	Na_VP: Control vs ATX-II	0.12 / 0.33	- / -

Table S2: Firing pattern passive properties (one-way 4-factor ANOVA)

Firing pattern	Current threshold (pA) (n)	V_{rest} (mV)	R_{in} (MΩ)	Cm (pF)
Sustained-A	133.3 ± 16.7 (3)	-60.0 ± 2.2 (6)	1020.0 ± 247.8 (5)	21.9 ± 2.3 (6)
Sustained-B	261.1 ± 26.1 (9)	-64.1 ± 1.8 (13)	852.2 ± 280.6 (9)	16.9 ±1.8 (12)
Sustained-C	295.5 ± 34.7 (11)	-63.5 ± 1.3 (10)	475.3 ± 128.8 (7)	15.1 ± 2.1 (9)
Transient	426.8 ± 33.9 (28)	-65.7 ± 0.9 (33)	464.9 ± 73.8 (20)	16.1 ± 1.1 (31)
p	0.001	0.11	0.08	0.18
power	0.94	0.51	0.56	0.41

Table S3: Direct comparisons of AP waveform differences (one-way 4-factor ANOVA)

	Current threshold (pA)		Spike height (V_{AP}) (mV)		Peak dV/dt (mV/ms)		AHP (mV)	
	p	Effect size	p	Effect size	p	Effect size	p	Effect size
Sustained-B vs Sustained-A	0.35		0.08		0.79		**0.009**	0.6
Sustained-C vs Sustained-A	0.58		0.05		0.31		**0.0005**	0.9
Sustained-C vs Sustained-B	0.95		0.98		0.71		0.46	
Transient vs Sustained-A	**0.01**	0.4	**0.004**	**0.6**	**0.01**	0.5	**0.000006**	1.0
Transient vs Sustained-B	**0.03**	0.4	0.66		**0.03**	0.3	**0.04**	0.5
Transient vs Sustained-C	0.08		0.92		0.58		0.77	

903

Table S4: Pharmacological effects on AP waveform (paired t-test)

4,9-ah-TTX	V_{rest} (mV) Transient	V_{rest} (mV) Sustained	Time-to-peak (ms)	Spike Width (ms)	AHP (mV)	V_{AP} (mV)	Voltage threshold (mV)	Peak dV/dt (mV/ms)
Control (n = 12)	-59.5 ± 1.5	-57.6 ± 3.3	4.1 ± 0.3	2.9 ± 0.5	0.0 ± 1.9	74.4 ± 6.4	-42.3 ± 2.3	102 ± 20
Drug	-63.6 ± 2.9	-66.8 ± 3.4	4.8 ± 0.4	3.9 ± 0.6	6.8 ± 1.2	55.1 ± 7.0	-43.3 ± 3.2	64.4 ± 20
p	0.16	**0.03**	**0.05**	0.13	**0.006**	**0.01**	0.90	**0.03**
Effect size		0.67	0.42	0.19	0.72	0.49	0.05	0.41
Power	0.27	0.67	0.53	0.31	0.86	0.76	0.05	0.62
ATX-II	V_{rest} (mV)							
Control (n = 7)	-59.2 ± 0.9		3.8 ± 0.3	1.2 ± 0.1	4.8 ± 0.8	92.7 ± 5.9	-49.7 ± 2.1	229 ± 30
Drug	-64.0 ± 2.2		5.5 ± 0.8	2.4 ± 0.6	4.1 ± 1.5	92.8 ± 6.3	-52.2 ± 3.5	209 ± 50
p	0.07		0.07	0.09	0.58	0.97	0.60	0.41
Effect size	0.83		0.45	0.35	0.10	0.01	0.23	0.14
Power	0.45		0.45	0.41	0.07	0.05	0.07	0.11

904

Table S5: Effects of increased I-Na$_V$T on spike rate and CV in mVGNs (p values from two-way 4-factor ANOVA)

	Spike Rate (Fig 10C)				CV (~38 spikes/s) (Fig 10 D)			
gNaT vs gNaT	Sus-A	Sus-B	Sus-C	Tran	Sus-A	Sus-B	Sus-C	Tran
16 14	3E-13	3E-08	1E-08	0.008	1	0.1	1	0.1
18 14	5E-22	3E-23	1E-18	4E-07	1	1E-05	0.3	0.04
18 16	0.001	3E-09	1E-04	0.2	1	0.1	1	1
20 14	7E-25	5E-30	2E-25	6E-12	0.3	5E-11	0.3	0.003
20 16	3E-06	1E-16	5E-11	8E-05	1	1E-05	1	1
20 18	1	0.0001	0.02	0.3	1	0.1	1	1
22 14	2E-27	5E-33	1E-29	1E-15	0.06	9E-13	1	2E-04
22 16	1E-08	3E-20	8E-16	5E-08	1	3E-07	1	1
22 18	0.1	6E-05	4E-06	0.001	1	0.01	1	1
22 20	1	1	0.4	1	1	1	1	1

905

906

Table S6: Effects of I-Na_VP and I-Na_VR on spike rate and CV in model VGNs driven by pseudo-EPSC trains (four-way 4-factor ANOVA)

		VGN: 2% P & 10% R			Calyx: 4% P & 20% R		
			vs. Na_VT			vs. Na_VT	
Spike Rate (spikes/s)		μ ± SEM	p	Effect size	μ ± SEM	p	Effect size
Sustained-A	Na_VT	82.2 ± 0.6	-		82.2 ± 0.6	-	
	Na_VT+R	81.5 ± 0.7	1		81.4 ± 0.6	1	
	Na_VT+P	83.9 ± 0.8	0.52		88.7 ± 0.6	**2E-08**	1.20
	Na_VT+R+P	85.5 ± 0.8	**0.01**	0.56	87.8 ± 0.6	**6E-07**	0.97
Sustained-B	Na_VT	65.9 ± 0.8	-		65.9 ± 0.8	-	
	Na_VT+R	64.5 ± 0.9	1		66.1 ± 0.9	1	
	Na_VT+P	67.8 ± 0.8	0.34		71.8 ± 0.6	**2E-06**	1.01
	Na_VT+R+P	68.9 ± 0.8	**0.03**	0.62	71.8 ± 0.9	**2E-06**	0.94
Sustained-C	Na_VT	57.9 ± 1.0	-		58.5 ± 1.0	-	
	Na_VT+R	58.1 ± 1.1	1		58.2 ± 1.2	1	
	Na_VT+P	61.3 ± 0.9	**0.01**	0.51	65.4 ± 0.9	**1E-07**	1.01
	Na_VT+R+P	62.3 ± 0.9	**0.0006**	0.61	66.5 ± 0.8	**2E-09**	1.19
Transient	Na_VT	29.5 ± 1.2	-		29.3 ± 1.1	-	
	Na_VT+R	29.9 ± 1.2	1		29.7 ± 1.2	1	
	Na_VT+P	32.1 ± 1.1	0.59		34.8 ± 1.1	**0.002**	0.72
	Na_VT+R+P	32.7 ± 1.3	0.26		35.7 ± 1.2	**0.0003**	0.82
CV (~38 spikes/s)		μ ± SEM	p	Effect size	μ ± SEM	p	Effect size
Sustained-A	Na_VT	0.22 ± 0.00	-		0.22 ± 0.02	-	
	Na_VT+R	0.24 ± 0.00	**0.03**	0.005	0.24 ± 0.02	**0.01**	0.01
	Na_VT+P	0.21 ± 0.00	0.06		0.19 ± 0.01	0.0004	0.01
	Na_VT+R+P	0.21 ± 0.00	0.1		0.20 ± 0.02	**0.02**	0.01
Sustained-B	Na_VT	0.43 ± 0.01	-		0.43 ± 0.01	-	
	Na_VT+R	0.46 ± 0.00	**0.03**	0.02	0.48 ± 0.01	**0.02**	0.01
	Na_VT+P	0.41 ± 0.01	**0.02**	0.01	0.38 ± 0.00	**0.002**	0.01
	Na_VT+R+P	0.42 ± 0.01	1		0.44 ± 0.01	1	
Sustained-C	Na_VT	0.51 ± 0.01	-		0.51 ± 0.01	-	
	Na_VT+R	0.56 ± 0.02	0.06		0.58 ± 0.02	**0.01**	0.02
	Na_VT+P	0.49 ± 0.01	1		0.47 ± 0.01	0.26	
	Na_VT+R+P	0.53 ± 0.01	1		0.53 ± 0.01	1	
Transient	Na_VT	0.60 ± 0.02	-		0.60 ± 0.03	-	
	Na_VT+R	0.61 ± 0.03	1		0.64 ± 0.03	1	
	Na_VT+P	0.57 ± 0.01	1		0.57 ± 0.01	1	
	Na_VT+R+P	0.57 ± 0.01	1		0.58 ± 0.01	1	

907